Dynamics of cable-driven parallel manipulators with variable length vibrating cables

Andrea Arena [a],[*], Erika Ottaviano [b], Vincenzo Gattulli [a]

[a] *Department of Structural and Geotechnical Engineering, Sapienza University of Rome, Via Eudossiana 18, Rome, 00184, Italy*
[b] *Department of Civil and Mechanical Engineering, University of Cassino and Southern Lazio, Via G. Di Biasio 43, Cassino (FR), 03043, Italy*

A B S T R A C T

A parametric nonlinear model of cable-driven parallel manipulators endowed with a three-dimensional end-effector is formulated and discussed in this paper. The proposed model considers the distributed stiffness, inertia, and damping of time-varying length cables and allows to study and characterize the dynamic response of manipulators equipped with a generic number n of cables. The equations of motion of each of the n cables are first derived via a total lagrangian formulation together with the compatibility equations prescribing the connectivity between the cables and the end-effector mass, while the dynamics of the end-effector are described by enforcing the balance of its linear and angular momentum. A discretization procedure, based on admissible trial functions, is used to reduce the nonlinear partial differential equations of motion of the cables to a set of ordinary differential equations. The resulting equations are coupled with those describing the motion of the end-effector and the approximate solution is calculated via numerical time integration. Direct and inverse dynamic problems are then formulated and solved for selected case-study manipulators; finally, the role on the dynamic response of the system of the main mechanical parameters and of the degree of over-actuation is discussed.

1. Introduction

Parallel robots are designed by multiple rigid links arranged in a parallel topology; these robots usually allow the end-effector (EE) to move in a three-dimensional (3D) space showing good dynamic performances and load capacity. Cable-Driven Parallel Manipulators (CDPMs) can be defined as parallel robots in which legs are replaced with extensible cables that allow to cover larger workspaces (WS) if compared to classical parallel robots. Cables are wound in actuated drums (i.e., the winches) that can be placed at a fixed frame, and the EE can be operated by controlling the cable lengths [1]. Several relevant works on CDPMs were initially based on the determination of the WS by referring to the so-called wrench-feasible workspace [2], that is, a set of mobile platform poses for which the cables can balance any wrench of a given set of wrenches, so that the tension in each cable remains within a prescribed range [3]. Therefore, the limits of the workspace is imposed by the highest load capacity for the upper bound, and by the cables slackness avoidance, for the lower bounds, initially considering as ideal cables with no mass and deformability.

In the analysis and design of CDPMs, an aspect of great importance to be considered is related to the number of active cables and their arrangement. For this reason, CDPMs were classified into two main categories, namely, over-constrained and under-constrained robots, respectively. In particular, over-constrained CDPMs were defined as robots having a number of actuated cables higher than the degrees of freedom (DOFs) of the EE, while under-constrained CDPMs are such that the cables cannot control all the DOFs of the robot. The latter category, includes cable suspended robots, defined as CDPMs for which all active cables are attached to the top of the suspended EE, while the bottom of the robot is free from cables. Since CDPMs have shown inherent advantages over conventional parallel robots, many applications were developed in the past and their use is continuously increasing. Works related to the low inertia for high-speed, pick-and-place, manipulators are reported in [4,5], while interesting examples of applications of CDPMs in large 3D workspaces are given by the NIST Robocrane [6] and by the skycam [7]. Further uses of parallel manipulators driven by cables include: material handling over large areas, positioning of heavy objects, rescue operations, mobility in urban environments [8], assistance, rehabilitation, entertainment [9], and also applications in huge telescopes, as the Five hundred meter Aperture Spherical Telescope (FAST) [10].

Cables are the main components of CDPMs; therefore, a deep understanding of their static and dynamic behaviors is fundamental to properly design these devices. However, the mechanical modeling of cables can be very challenging if considering both their distributed mass, elasticity, and damping properties [11–14]. Within this context,

richest dynamical models of elastic cables, including the bending and the torsional stiffness, were proposed in [15–17] and the identification of the axial and bending stiffness in stay cables was also performed in [18], while the effects of the temperature in the elastic response of cable were investigated in [19]. Those models have found suitable applications in the study and the characterization of the static and the dynamic behavior of CDPMs. In particular, the Irvine cable model [11] was adopted, as first, to formulate and solve the kinetostatic problem of CDPMs for studying the effect of the cables sag [20,21], while more sophisticated nonlinear models, including the three-dimensional description of the finite kinematics and the large deformation of elastic cables, were proposed in [22–24] to solve the direct and the inverse kinematic problems of CDPMs working in a 3D space.

For what concerns the dynamics of CDPMs, in early studies, the distributed inertia and stiffness of cables were typically neglected since those were modeled via massless, rigid, links able at moving the EE in space [25]. In [26,27] elastic cables were modeled, first, as springs and, then, as taut strings, for studying the effect of the cables distributed elasticity and its influence in the dynamic response of moving platforms. In [28], the kinematics and the dynamics of the IPAnema3 cable robot were studied by modeling each cable as a spring–damper rheological element with variable stiffness and damping given by the change in the effective cable length. Nevertheless, this assumption may not be accurate, especially for CDPMs with heavy and/or very long cables. Within this context, geometric curvature, i.e., the cable sag, plays an important role in the mechanical response of the cables and of the whole CDPM, this is because it represents a source of non-negligible stiffness, also known as geometric stiffness, which may influence the static and dynamic behavior even more than the elastic axial stiffness itself [29,30].

Most of the works available in the literature consider both, the cable elastic and geometric stiffness, and the distributed mass, to study the free-vibrations of two-dimensional CDPMs characterized by inclined cables [29,31]. The vibrations of the moving platform of CDPMs with large workspaces were studied in [32,33], where cables were modeled by including their distributed mass and axial stiffness and the equations of motion were solved by using different numerical techniques, e.g., converting to ordinary differential equations by using finite element method [32] and by means of the assumed-mode method [33,34], respectively. Within this context, the correct modeling of the cable stiffness and inertia plays a fundamental role and has significant effects both in the static and in the dynamic response of CDPMs, such as in the correct kinematic description of the motion, the EE positioning accuracy, the forces distribution in the cables, and in the vibration and the control of the robot. In [35] an adaptive control of robot manipulators with kinematic uncertainties is proposed for parallel robots based on the representation of the Jacobian matrix in regressor form with asymptotic trajectory tracking, while in [36] a vision-based method is presented for cable-driven robots to simultaneously measure the manipulator configuration and the target pose. In [28] static and dynamic stiffness analyses of CDPMs were performed by including a static sagging cable model, which considers the cable mass and elasticity, and describes the static cable profile by a set of nonlinear equations. The proposed model is based on the Dynamic Stiffness Matrix (DSM) method. A further suitable approach for modeling the effect of the mass of the cables is to consider those as chains having lumped masses connected by elastic links instead of modeling them as one-dimensional elastic continua. To this end, planar models were developed in [37,38] where it was assumed that the cable mass was lumped at selected locations (called the nodes) along its configuration. The axial stiffness and the damping properties of a segment falling in between a pair of nodes were modeled as an equivalent spring–damper element, in place of the physical segment. A similar model, accounting for the spatial motions of the cables, was used in [39] for controlling the receiver of a radio telescope supported by an aerostat, and in [8], where a large CDPM was modeled to

position a cabin in space. A spatial model of CDPM, proposed in [40], incorporated the mass and the elasticity of the cable in the longitudinal, transverse, and lateral directions, respectively, to investigate the role of such parameters in the 3D dynamic response of the mechanical system. In [41], the static and dynamic stiffness of CDPMs were characterized and studied in a 3D space. To this end, by starting from the inclined cables configuration at the equilibrium, the forced vibrations of the inclined cables were studied by combining static and dynamic equilibrium configurations. One of the issues related to the use of discrete models is that, in order to provide a good approximation of the mechanical continuum, a sufficiently large number of elements is required. However, when the number of elements increase, then the degrees-of-freedom of the system increase proportionally, leading to computational challenges. Considering the elasticity along different directions, the cables were modeled as Reissner beams in [42], and used for the simulation and the control of the CoGiRo robot with the help of XDE and MATLAB/Simulink [43]; the experimental validation of the above-mentioned numerical simulations was then presented in [44]. A more sophisticated cable model, based on the Cosserat theory of rods, was adopted in [34] to calculate the natural frequencies of a planar 4–4 CDPM with time-varying cable lengths, while, in [45] was presented an Arbitrary Lagrange Euler (ALE) method for the dynamic modeling and simulation of cable-driven mechanisms considering stick–slip frictions. Similar to the discrete models of the cables, the accuracy of continuum-based models is limited by the number of finite elements that can be practically used, as mentioned in [42,43], or equivalently, of the degrees of the Bernstein polynomials used in [34] for approximating the solution of the partial differential equations describing the dynamics of the system. Indeed, the numerical simulation of the CDPM dynamics implies the analysis of systems having large number of DOF and multiple closed-loops. Typically, the formulations adopted to overcome the computational drawbacks are based on the recursive Newton–Euler formulation (NEF) and on the constrained lagrangian formulation (CLF), or hybrid NEF/CLF formulations, which allow to account for the coupling between the dynamics of the cables and the motion of the EE. An improved forward dynamic algorithm, known as the sub-system-level lagrangian multiplier (SSLM) approach, was proposed in [46], and it was specifically developed for systems having multiple closed-loops. The same theoretical framework was adopted in [47] to be applied to FAST and CoGiRo robots; moreover, the model was improved to reduce the overall computational costs arising from the use of a recursive algorithm for the optimal computation of the Lagrange multipliers.

In the present paper, a parametric nonlinear dynamic model of CDPMs undergoing three-dimensional motions is presented and discussed, and the solution of both, the direct and the inverse dynamic problems, is provided my means of a discretization procedure based on admissible trial functions. The novelties of this work can be summarized as follows: i. the formulation of an analytical procedure to model and solve the dynamic problem of CDPMs endowed with a 3D end-effector and including the effects of the distributed stiffness, inertia, and damping of the cables; ii. providing a solution strategy based on an *ad hoc* nondimensionalization of the system parameters and equations able at overcoming the analytical and numerical drawbacks related to the time-varying length of the cables; iii. providing and discussing solution strategies for both, direct and inverse, dynamic problems in the case of minimally-actuated and over-actuated systems.

2. Nonlinear parametric modeling

Hereinafter, a nonlinear dynamic model of cable-driven parallel manipulator (CDPM) including the elasticity of the cables and their distributed mass is presented and discussed. The CDPM model is formulated by considering a generic number n of cables whose length is varied in time to move and to change the orientation of an end-effector (EE) mass in a three-dimensional (3D) space by means of prescribed trajectories. In particular, the EE is first described as an
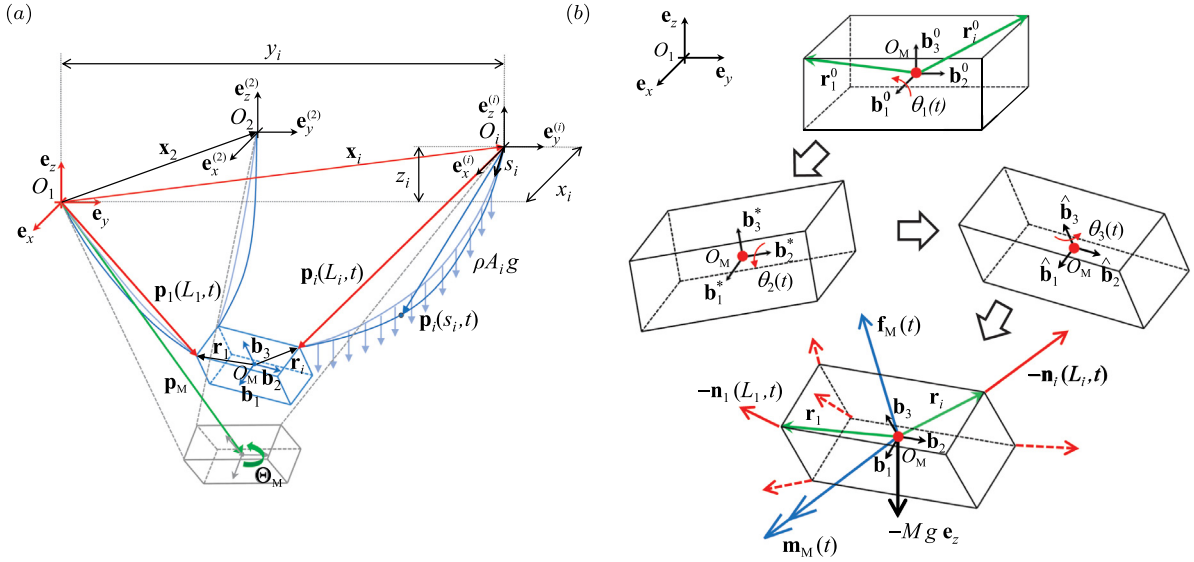
Fig. 1. (a) Schematic representation of the CDPM: target configuration (gray) vs configuration calculated via Direct approach (blue). (b) Finite rotations and equilibrium of the forces acting on the end-effector mass. (For interpretation of the references to color in this figure legend, the reader is referred to the web version of this article.)

orientable 3D rigid body having a generic shape and, then, the case of a point-mass end-effector is further derived and discussed in the work. An exact geometric formulation of the cable dynamics is derived by accounting for finite displacements and rotations of the end-effector, and the strong form of the system's equations of motion is then derived via a Lagrangian formulation. The nonlinear differential equations of motion of the cables, coupled with the balance equations of the linear and angular momentum of the EE, are then solved by seeking an approximate numerical solution using admissible trial functions.

The notation used for the mathematical formulation adopted in this work considers vectors and matrices as elements of the real coordinate 3D space $\mathbb{R}^3$; moreover, vector-valued functions are denoted by lower-case, bold-face symbols, while matrices are represented by capital-case, boldface symbols, and scalar functions are denoted by lower-case, italic symbols. Furthermore, the cross product of vectors is denoted by the symbol $\times$ and the transpose operator by the superscript $\top$. Finally, the Leibniz's notation $\frac{d}{dx}(\cdot)$ is used for derivatives in terms of a generic dimensional variable x, while the Lagrange's notation $(\cdot)'$ and the Newton's notation $(\dot{\cdot})$ are adopted for derivatives with respect to the nondimensional space and time variables, respectively.

2.1. Kinematic formulation

The analytical model of the ith elastic cable with distributed mass is parametrized in time by means of the variable t and in space by adopting the cable arclength $s_i \in [0, L_i(t)]$ $(i = 1, \ldots, n)$ of the unstretched configuration, where $L_i(t)$ is the time-varying total unstretched length of the ith cable. Moreover, at time t, the minimum distance between the boundaries of the ith cable is given by $l_i(t)$. As shown in Fig. 1(a), the geometry and the kinematics of the system are described by considering n fixed Cartesian frames having origin positioned at the boundary $s_i = 0$ of the corresponding cable. The origins of the n frames are positioned in the frame $(\mathbf{e}_x, \mathbf{e}_y, \mathbf{e}_z)$, being $\mathbf{e}_z$ the gravity direction, and centered in the point O_1 of the first cable (i.e., at $s_1 = 0$), by the 3-by-1 position vector $\mathbf{x}_i = [x_i \; y_i \; z_i]^\top$ $(i = 1, \ldots, n)$; therefore, it turns out that $\mathbf{x}_1 \equiv \mathbf{0}$, where $\mathbf{0}$ is the null vector.

At time t, the vector describing, in the fixed frame $(\mathbf{e}_x, \mathbf{e}_y, \mathbf{e}_z)$, the position of the point belonging to the end-effector and connected to the ith cable is $\mathbf{r}_i(t) = \Theta(t)\mathbf{r}_i^0$, where $\mathbf{r}_i^0$ is the position vector in the mass-fixed local frame $(\mathbf{b}_1(t), \mathbf{b}_2(t), \mathbf{b}_3(t))$ centered in the EE center of mass O_M. The operator $\Theta(t)$ is the 3-by-3 time-dependent orthogonal matrix obtained by considering the Tait–Bryan angles $\theta_k(t)$ $(k = 1, 2, 3)$

and assuming the following sequence of finite rotations (see Fig. 1(b)): $\theta_1(t)$, about the axis $\mathbf{b}_1^0 \equiv \mathbf{e}_x$, $\theta_2(t)$, about the axis $\mathbf{b}_2^*$, and $\theta_3(t)$, about the axis $\hat{\mathbf{b}}_3 \equiv \mathbf{b}_3(t)$. Hence, the finite rotations matrix can be written as

$$\Theta(t) = \begin{bmatrix} c_2 c_3 & -c_2 s_3 & s_2 \\ c_1 s_3 + s_1 s_2 c_3 & c_1 c_3 - s_1 s_2 s_3 & -s_1 c_2 \\ s_1 s_3 - c_1 s_2 c_3 & s_1 c_3 + c_1 s_2 s_3 & c_1 c_2 \end{bmatrix}, \tag{1}$$

where s_k and c_k indicate $\sin \theta_k(t)$ and $\cos \theta_k(t)$, respectively, for $k = 1, 2, 3$.

To describe the position of the material point on the ith cable is adopted the vector $\mathbf{p}_i(s_i, t) = [p_{x,i}(s_i, t) \; p_{y,i}(s_i, t) \; p_{z,i}(s_i, t)]^\top$ whose components are defined in the ith fixed frame and where s_i represents the unstretched arclength of the ith cable (see Fig. 1). The strain state of the ith cable can be described by introducing the stretch vector $\mathbf{v}_i(s_i, t)$ calculated as $\mathbf{v}_i(s_i, t) = \frac{d}{ds_i}\mathbf{p}_i(s_i, t)$, and whose norm has the following expression in terms of the components of the position vector $\mathbf{p}_i(s_i, t)$:

$$v_i(s_i, t) = \sqrt{\left(\frac{dp_{x,i}}{ds_i}\right)^2 + \left(\frac{dp_{y,i}}{ds_i}\right)^2 + \left(\frac{dp_{z,i}}{ds_i}\right)^2}. \tag{2}$$

Therefore, the unit vector $\mathbf{a}_i$, providing the axial direction tangent to the dynamic configuration of the ith cable, can be straightforwardly calculated as $\mathbf{a}_i(s_i, t) = \mathbf{v}_i(s_i, t)/v_i(s_i, t)$.

2.2. Equations of motion

To derive the strong form of the equations of motion of the CDPM it is first necessary to introduce the expression of the vector of the internal forces of the ith cable at position s_i and time t. By considering purely extensible cables, this vector collects only the axial force and it has the following expression: $\mathbf{n}_i(s_i, t) = N_i(s_i, t)\mathbf{a}_i(s_i, t)$, where the tension $N_i(s_i, t)$ can be calculated as $N_i(s_i, t) = EA_i(v_i(s_i, t) - 1)$, being EA_i the axial stiffness of the ith cable. It is worth mentioning that, in the here considered mechanical model, the constitutive behavior of the extensible cables is assumed to be linearly elastic; therefore, only geometric nonlinearities govern the dynamic response of the system.

The equation of motion of the ith cable can be derived according to the first Euler law of motion by enforcing the balance of linear momentum and can be written, in vector-valued form, as

$$\frac{d}{ds_i}\mathbf{n}_i(s_i, t) + \mathbf{f}_i(s_i, t) = \rho A_i \frac{d^2}{dt^2}\mathbf{p}_i(s_i, t) + c_i \frac{d}{dt}\mathbf{p}_i(s_i, t) \quad (i = 1, \ldots, n), \tag{3}$$

where $\mathbf{f}_i(s_i, t)$ is the vector collecting the forces per unit length acting on the cable, while ρA_i is the mass per unit length of the ith cable,

respectively. Moreover, the Rayleigh dissipation function is considered to model the damping and the damping coefficient c_i is here assumed to be $c_i = 2\zeta\sqrt{EA_i\,\rho A_i/l_{0,1}^2}$, where ζ is a damping factor. Eq. (3) is a second-order, in space and in time, differential equation whose unknown is the vector-valued function $\mathbf{p}_i(s_i, t)$ which must satisfy the following kinematic boundary conditions at $s_i = 0$:

$$\mathbf{p}_i(0, t) = \mathbf{0} \quad (i = 1, \ldots, n), \tag{4}$$

for assigned initial conditions.

The overall dynamics of the CDPM, consisting of n cables connected to the end-effector, are described by n vector-valued functions $\mathbf{p}_i(s_i, t)$ $(i = 1, \ldots, n)$ which are solution of the corresponding equation of motion of the type given by Eq. (3); the ith kinematic unknown must then satisfy the following relationship:

$$\mathbf{x}_i + \mathbf{p}_i(L_i, t) - \mathbf{r}_i(t) = \mathbf{p}_1(L_1, t) - \mathbf{r}_1(t) \quad (i = 2, \ldots, n), \tag{5}$$

which provides, at time t, the compatibility condition ensuring that the material point at $s_i = L_i(t)$ of each cable is connected to the end-effector at the position $\mathbf{r}_i(t)$ from the center of mass O_M. Finally, to ensure the balance of the linear momentum of the end-effector mass M, the following vector-valued equation holds:

$$-\sum_{i=1}^{n} \mathbf{n}_i(L_i, t) - Mg\,\mathbf{e}_z = \mathbf{f}_M(t), \tag{6}$$

where $\mathbf{f}_M(t) = M\left[\frac{d^2}{dt^2}\left(\mathbf{p}_1(L_1, t) - \mathbf{r}_1(t)\right)\right]_{(s_1 = L_1, t)}$ is the time rate of change of the end-effector linear momentum, and the difference vector $\mathbf{p}_1(L_1, t) - \mathbf{r}_1(t)$ provides the position of the end-effector center of mass O_M in the fixed frame $(\mathbf{e}_x, \mathbf{e}_y, \mathbf{e}_z)$. On the other hand, the balance of the angular momentum of the EE is given by

$$-\sum_{i=1}^{n} \mathbf{r}_i(t) \times \mathbf{n}_i(L_i, t) = \mathbf{m}_M(t), \tag{7}$$

where $\mathbf{m}_M(t) = \boldsymbol{\Theta}(t)\left(\mathbf{J}_M \frac{d}{dt}\boldsymbol{\omega}(t)\right)$ is the time rate of change of the end-effector angular momentum, and $\mathbf{J}_M$ is the diagonal matrix of the principal mass moment of inertia with respect to the end-effector mass-fixed local frame $(\mathbf{b}_1(t), \mathbf{b}_2(t), \mathbf{b}_3(t))$, while the components of the 3-by-1 vector $\boldsymbol{\omega}(t) = [\omega_1(t)\ \omega_2(t)\ \omega_3(t)]^\top$, which collects the angular velocities about the axes of the local frame, are the non-trivial components of the skew-symmetric matrix $\boldsymbol{\Omega}(t) = \boldsymbol{\Theta}(t)^\top(d\boldsymbol{\Theta}(t)/dt)$ and have the following expressions:

$$\begin{aligned}
\omega_1(t) &= \frac{d\theta_1}{dt}\cos\theta_2\cos\theta_3 + \frac{d\theta_2}{dt}\sin\theta_3, \\
\omega_2(t) &= \frac{d\theta_2}{dt}\cos\theta_3 - \frac{d\theta_1}{dt}\cos\theta_2\sin\theta_3, \\
\omega_3(t) &= \frac{d\theta_3}{dt} + \frac{d\theta_1}{dt}\sin\theta_2.
\end{aligned} \tag{8}$$

2.3. End-effector trajectory

The trajectory of the end-effector, including its orientation, can be described through the position of the center of mass, given by the vector $\mathbf{p}_M(t)$, and the rotation of the local frame $(\mathbf{b}_1(t), \mathbf{b}_2(t), \mathbf{b}_3(t))$ given by the matrix $\boldsymbol{\Theta}(t)$. Therefore, the position of each connected point of the end-effector is provided, in the fixed frame $(\mathbf{e}_x, \mathbf{e}_y, \mathbf{e}_z)$, by the vector $\mathbf{p}_{M,i}(t)$ whose expression can be calculated as:

$$\mathbf{p}_{M,i}(t) = \mathbf{p}_M(t) + \boldsymbol{\Theta}(t)\mathbf{r}_i^0 - \mathbf{x}_i \quad (i = 1, \ldots, n). \tag{9}$$

Hence, at time t, the distance between the boundary points of the ith cable can be calculated as:

$$l_i(t) = \sqrt{\mathbf{p}_{M,i}(t)^\top \mathbf{p}_{M,i}(t)} \quad (i = 1, \ldots, n). \tag{10}$$

It is necessary to highlight that feasible initial positions and orientations of the EE mass must be provided within the so-called workspace of the CDPM. This mainly depends on the geometry of the CDPM and its characterization can be done via static analyses; further details on the definition of suitable 3D workspaces of CDPMs can be found in [24,48].

3. Nondimensional form

The solution of the equations of motion of the n cables and that of the balance equations of the EE linear and angular momentum turns out to be an arduous task to be achieved due to the time varying space domains (i.e., $s_i \in [0, L_i(t)]$) characterizing the mechanical system. Nevertheless, a suitable nondimensionalization of the differential equations and of the system geometrical and mechanical parameters can provide a valid stratagem to overcome this issue. To this end, the distance $l_{0,1} = l_1(0)$, at time $t = 0$, between the boundary points of the first cable (i.e., $i = 1$) is adopted as characteristic length to rescale, in space, the mechanical problem, while the characteristic frequency $\omega_c = \sqrt{EA_1/\left(\rho A_1\,l_{0,1}^2\right)}$ is adopted to nondimensionalize the time, where EA_1 and ρA_1 are the axial stiffness and the mass per unit length of the first cable, respectively. Therefore, the following scalar and vector-valued nondimensional parameters can be introduced:

$$\begin{aligned}
&\lambda_{0,i} = \frac{l_{0,i}}{l_{0,1}}, \ \bar{\mathbf{x}}_i = \frac{\mathbf{x}_i}{l_{0,1}}, \ \bar{\mathbf{r}}_i^0 = \frac{\mathbf{r}_i^0}{l_{0,1}}, \ \bar{\mathbf{r}}_i = \frac{\mathbf{r}_i}{l_{0,1}}, \\
&\bar{\mathbf{p}}_M = \frac{\mathbf{p}_M}{l_{0,1}}, \ \bar{\mathbf{p}}_i = \frac{\mathbf{p}_i}{l_{0,1}}, \ \bar{\mathbf{n}}_i = \frac{\mathbf{n}_i}{\rho A_1\,\omega_c^2\,l_{0,1}^2}, \ (i = 1\ldots n),
\end{aligned} \tag{11}$$

being $\rho A_1\,\omega_c^2\,l_{0,1}^2 \equiv EA_1$ a characteristic force and $\lambda_{0,1} \equiv 1$; on the other hand, the nondimensional time τ can be calculated as $\tau = \omega_c\,t$. Finally, the following nondimensional time-varying parameters are defined:

$$\lambda_i(\tau) = \frac{l_i(\tau)}{l_{0,i}}, \ \Lambda_i(\tau) = \frac{L_i(\tau)}{l_i(\tau)}, \tag{12}$$

where $\lambda_i(\tau)$ is the ratio between the boundary points of the ith cable at time τ and the corresponding length at $\tau = 0$, while $\Lambda_i(\tau)$ is the time-varying aspect ratio of the ith cable. Note that, at time $\tau = 0$, $\lambda_i(0) = 1$ for all i, which, for $i > 1$, does not necessary correspond to the value of $\lambda_{0,i}$.

Differently from what it was done for the system position vectors, to rescale the space coordinate s_i it is convenient to adopt a different nondimensionalization criterion and to introduce the nondimensional arclength $\sigma = s_i/L_i(t)$, which varies into the nondimensional domain $[0, 1]$ at any time τ. Based on the expressions introduced in Eq. (12), it turns out that $L_i(\tau) = \Lambda_i(\tau)\lambda_i(\tau)l_{0,i}$; therefore, the derivative with respect to the ith dimensional arclength s_i can be calculated in terms of the nondimensional arclength σ as

$$\frac{d}{ds_i}(\cdot) = \frac{1}{\Lambda_i(\tau)\lambda_i(\tau)l_{0,i}}(\cdot)', \tag{13}$$

while the time derivative can be calculated in terms of the nondimensional time τ as $\frac{d}{dt}(\cdot) = \omega_c(\dot{\cdot})$, being $(\cdot)' := \frac{d}{d\sigma}(\cdot)$ and $(\dot{\cdot}) := \frac{d}{d\tau}(\cdot)$, respectively. Hence, in terms of the nondimensional parameters and variables, the stretch vector can be then calculated as $\mathbf{v}_i(\sigma, \tau) = \bar{\mathbf{p}}_i'(\sigma, \tau)/\left(\Lambda_i(\tau)\lambda_i(\tau)\lambda_{0,i}\right)$, and the corresponding norm as $v_i(\sigma, \tau) = \sqrt{\left(\bar{p}_{x,i}'\right)^2 + \left(\bar{p}_{y,i}'\right)^2 + \left(\bar{p}_{z,i}'\right)^2}/\left(\Lambda_i(\tau)\lambda_i(\tau)\lambda_{0,i}\right)$ $(i = 1, \ldots, n)$.

Due to the definition of ω_c, it turns out that the ith axial force is given in nondimensional form as $\bar{N}_i(\sigma, \tau) = \kappa_i(v_i(\sigma, \tau) - 1)$, where $\kappa_i = \left(EA_i/EA_1\right)$ is the nondimensional axial stiffness of the ith cable, defined as the ratio between the stiffness of the ith cable and that of the first cable; therefore, the corresponding vector of the nondimensional axial force can be written as

$$\bar{\mathbf{n}}_i(\sigma, \tau) = \frac{\kappa_i}{\Lambda_i(\tau)\lambda_i(\tau)\lambda_{0,i}} \frac{\left(v_i(\sigma, \tau) - 1\right)}{v_i(\sigma, \tau)}\bar{\mathbf{p}}_i'(\sigma, \tau). \tag{14}$$

Finally, the equation of motion of the ith cable in nondimensional, vector-valued form reads

$$\frac{\bar{\mathbf{n}}_i'(\sigma, \tau)}{\Lambda_i(\tau)\lambda_i(\tau)\lambda_{0,i}} + \bar{\mathbf{f}}_i(\sigma, \tau) = \varrho_i\ddot{\bar{\mathbf{p}}}_i(\sigma, \tau) + \bar{c}_i\dot{\bar{\mathbf{p}}}_i(\sigma, \tau) \quad (i = 1, \ldots, n), \tag{15}$$

where $\varrho_i = \rho A_i/\rho A_1$ is the ratio between the mass per unit length of the ith and that of the first cable, and $\bar{c}_i = c_i/\left(\rho A_1\omega_c\right)$ is the

nondimensional damping coefficient. The nondimensional distributed load, calculated as $\bar{\mathbf{f}}_i = \mathbf{f}_i / \left(\rho A_1 \omega_c^2 l_{0,1} \right)$, is here considered to be only the cable self-weight, i.e., $\mathbf{f}_i = -\rho A_i\, g\, \mathbf{e}_z$, where $g = 9.81\ \text{m/s}^2$ is the gravity acceleration; therefore, in Eq. (15), $\bar{\mathbf{f}}_i = -\varrho_i\, \gamma\, \mathbf{e}_z$, where $\gamma = g / \left(\omega_c^2\, l_{0,1} \right)$. Finally, Eqs. (4) and (5) can be rewritten in nondimensional form as

$$\bar{\mathbf{p}}_i(0, \tau) = \mathbf{0} \quad (i = 1, \dots, n), \tag{16}$$

$$\bar{\mathbf{x}}_i + \bar{\mathbf{p}}_i(1, \tau) - \bar{\mathbf{r}}_i(\tau) = \bar{\mathbf{p}}_1(1, \tau) - \bar{\mathbf{r}}_1(\tau) \quad (i = 2, \dots, n), \tag{17}$$

respectively, while the nondimensional form of the vector-valued balance equations of the end-effector linear and angular momentum can be written as

$$-\sum_{i=1}^{n} \bar{\mathbf{n}}_i(1, \tau) - \mu\, \gamma\, \mathbf{e}_z = \mu \left(\ddot{\bar{\mathbf{p}}}_1(1, \tau) - \ddot{\bar{\mathbf{r}}}_1(\tau) \right), \tag{18}$$

$$-\sum_{i=1}^{n} \left(\bar{\mathbf{r}}_i(\tau) \times \bar{\mathbf{n}}_i(1, \tau) \right) = \boldsymbol{\Theta}(\tau) \left(\bar{\mathbf{J}}_\mu\, \dot{\boldsymbol{\omega}}(\tau) \right), \tag{19}$$

respectively, where $\mu = M / \left(\rho A_1\, l_{0,1} \right)$ represents the nondimensional EE mass and $\bar{\mathbf{J}}_\mu = \mathbf{J}_M \left[1 / \left(\rho A_1\, l_{0,1}^3 \right) \right] = \mu\, \text{diag} \left(\bar{I}_{P1}, \bar{I}_{P2}, \bar{I}_{P3} \right)$, where $\text{diag}\,(\cdot)$ represents a diagonal matrix and $\bar{I}_{P1}$, $\bar{I}_{P2}$, $\bar{I}_{P3}$, are the nondimensional polar moments of inertia of the end-effector with respect to the axes $\mathbf{b}_1(t)$, $\mathbf{b}_2(t)$, and $\mathbf{b}_3(t)$, respectively. In the present work, the inertial and the elastic parameters (i.e., ρA_i and EA_i, respectively) are assumed to be the same for all n cables, therefore $\kappa_i = 1$ and $\varrho_i = 1$ $(i = 1, \dots, n)$.

It is worth noting that, differently from Eq. (3), Eq. (15) is a vector-valued partial differential equation having time-varying coefficients. Nevertheless, although the nondimensionalization entailed a more elaborated writing of the equations of motion, the use of nondimensional variables will provide indisputable advantages in the numerical treatment and in the calculation of the solution of Eq. (15), as discussed in the next.

3.1. Approximate solution of the equations of motion

The discretization technique based on the use of admissible trial functions is adopted to reduce the space-dependence of the equations of motion of the cables so as to reduce them into a set of ordinary differential equations, in the nondimensional time variable τ, coupled with the boundary equations of the balance of the end-effector linear and angular momentum. To this end, $m + 1$ trial functions are chosen to satisfy the kinematic boundary conditions (16) and (17); therefore, the approximate solution of Eq. (15) is given by the 3-by-1 vector $\tilde{\mathbf{p}}_i(\sigma, \tau)$ $(i = 1, \dots, n)$ expressed as the linear combination of the $m + 1$ trial functions as

$$\tilde{\mathbf{p}}_i(\sigma, \tau) = \mathbf{q}_{i,0}(\tau)\, \sigma + \sum_{j=1}^{m} \boldsymbol{\phi}_{i,j}(\sigma)\, \mathbf{q}_{i,j}(\tau), \tag{20}$$

where $\boldsymbol{\phi}_{i,j}(\sigma) = \text{diag} \left(\varphi_{i,j}^{(x)}(\sigma), \varphi_{i,j}^{(y)}(\sigma), \varphi_{i,j}^{(z)}(\sigma) \right)$ is the ijth 3-by-3 diagonal matrix collecting the jth trial functions used to discretize the components of the ith solution vector along the directions $\mathbf{e}_x$, $\mathbf{e}_y$, and $\mathbf{e}_z$, respectively. In particular, it is assumed that $\varphi_{i,j}^{(x)}(\sigma) = \varphi_{i,j}^{(y)}(\sigma) = \varphi_{i,j}^{(z)}(\sigma) = \sin(j\,\pi\,\sigma)$, thus adopting the trigonometric function $\sin(j\,\pi\,\sigma)$ as the jth trial function to approximate all components of the n solution vectors. Finally, $\mathbf{q}_{i,0} = \left[q_{i,0}^{(x)}\ q_{i,0}^{(y)}\ q_{i,0}^{(z)} \right]^\top$ and $\mathbf{q}_{i,j} = \left[q_{i,j}^{(x)}\ q_{i,j}^{(y)}\ q_{i,j}^{(z)} \right]^\top$ are the vectors collecting the unknown generalized coordinates.

It is evident that, due to the trial functions considered in the discretization, Eq. (20) satisfies Eq. (16) since $\tilde{\mathbf{p}}_i(0, \tau) = \mathbf{0}$, whereas, to satisfy the compatibility equation Eq. (17), the following relationship must hold:

$$\mathbf{q}_{i,0}(\tau) = \mathbf{q}_{1,0}(\tau) - \bar{\mathbf{r}}_1 + \bar{\mathbf{r}}_i - \bar{\mathbf{x}}_i \quad (i = 2, \dots, n), \tag{21}$$

since $\sin(j\,\pi\,\sigma) = 0$ at $\sigma = 1$ for all j. Therefore, only one out of n vectors $\mathbf{q}_{i,0}(\tau)$ is an independent set of unknown coordinates, and those are given by the vector $\mathbf{q}_{1,0}(\tau)$.

By now substituting the approximate solution (20) into the equation of motion (15), the following vector of the unbalanced residual of the ith equation of motion can be calculated:

$$\tilde{\boldsymbol{\eta}}_i(\sigma, \tau) = \frac{\kappa_i}{\Lambda_i^2\, \lambda_i^2\, \lambda_{0,i}^2} \left[\frac{(\tilde{\nu}_i - 1)}{\tilde{\nu}_i} \tilde{\mathbf{p}}_i' \right]' + \bar{\mathbf{f}}_i - \varrho_i\, \ddot{\tilde{\mathbf{p}}}_i - \bar{c}_i\, \dot{\tilde{\mathbf{p}}}_i \quad (i = 1, \dots, n), \tag{22}$$

where $\tilde{\nu}_i$ is the stretch of the ith cable evaluated in terms of the approximate solution and the nondimensional space and time dependence of the expressions in the right-hand side of Eq. (22) was dropped for the sake of notation. It is a matter of fact that, when $m \neq \infty$, the residual of the ith equation of motion is non-null, i.e., $\tilde{\boldsymbol{\eta}}_i(\sigma, \tau) \neq \mathbf{0}$ $(i = 1, \dots, n)$; therefore, to minimize the n vectors of the unbalanced residuals given by Eq. (22), the former are first weighted by means of the trial functions adopted to approximate the solution and, then, their integral in the nondimensional space domain is set to zero. To this end, by collecting the n vectors of the unbalanced residuals into the $3n$-by-$3n$ diagonal matrix $\tilde{\mathbf{H}}(\sigma, \tau) = \text{diag}(\tilde{\eta}_1^{(x)}, \tilde{\eta}_1^{(y)}, \tilde{\eta}_1^{(z)}, \dots, \tilde{\eta}_n^{(x)}, \tilde{\eta}_n^{(y)}, \tilde{\eta}_n^{(z)})$, and by introducing the following $3n$-by-m matrix $\boldsymbol{\Phi}(\sigma)$ collecting the $3\,n\,m$ trial functions

$$\boldsymbol{\Phi}(\sigma) = \begin{bmatrix} \varphi_{1,1}^{(x)}(\sigma) & \cdots & \varphi_{1,m}^{(x)}(\sigma) \\ \varphi_{1,1}^{(y)}(\sigma) & \cdots & \varphi_{1,m}^{(y)}(\sigma) \\ \varphi_{1,1}^{(z)}(\sigma) & \cdots & \varphi_{1,m}^{(z)}(\sigma) \\ \vdots & \ddots & \vdots \\ \varphi_{n,1}^{(x)}(\sigma) & \cdots & \varphi_{n,m}^{(x)}(\sigma) \\ \varphi_{n,1}^{(y)}(\sigma) & \cdots & \varphi_{n,m}^{(y)}(\sigma) \\ \varphi_{n,1}^{(z)}(\sigma) & \cdots & \varphi_{n,m}^{(z)}(\sigma) \end{bmatrix}, \tag{23}$$

the matrix $\tilde{\mathbf{H}}(\sigma, \tau)$ of the unbalanced residuals can be minimized by ensuring that it is orthogonal, in the nondimensional domain $[0, 1]$, to the trial functions adopted in the discretization, that is:

$$\int_0^1 \boldsymbol{\Phi}(\sigma)^\top \tilde{\mathbf{H}}(\sigma, \tau)\, d\sigma = \mathbf{O}, \tag{24}$$

where $\mathbf{O}$ is a m-by-$3n$ zero matrix. Finally, the approximate form of the vector-valued balance equations of the end-effector can be written as

$$\sum_{i=1}^{n} \tilde{\mathbf{n}}_i(1, \tau) + \mu\, \gamma\, \mathbf{e}_z + \mu \left(\ddot{\tilde{\mathbf{p}}}_1(1, \tau) - \ddot{\bar{\mathbf{r}}}_1(\tau) \right) = \mathbf{0}, \tag{25}$$

$$\sum_{i=1}^{n} \left(\bar{\mathbf{r}}_i(\tau) \times \tilde{\mathbf{n}}_i(1, \tau) \right) + \boldsymbol{\Theta}(\tau) \left(\bar{\mathbf{J}}_\mu\, \dot{\boldsymbol{\omega}}(\tau) \right) = \mathbf{0}, \tag{26}$$

where $\tilde{\mathbf{n}}_i(1, \tau)$ is the approximate axial force vector calculated at $\sigma = 1$.

3.1.1. Initial equilibrium

In order to calculate the solution of the CDPM equations of motion, initial conditions must be enforced for the unknown variables and these can be calculated by solving the equilibrium of the system at time $\tau = 0$. To this end, the equilibrium equations can be derived from Eqs. (24), (25), and (26), by setting to zero the inertia and the dissipative terms, respectively; hence the vector-valued equilibrium equations in terms of the generalized coordinates read:

$$\int_0^1 \boldsymbol{\Phi}(\sigma)^\top \tilde{\mathbf{H}}^0(\sigma)\, d\sigma = \mathbf{O},$$
$$\sum_{i=1}^{n} \tilde{\mathbf{n}}_i^0(1) + \mu\, \gamma\, \mathbf{e}_z = \mathbf{0}, \tag{27}$$
$$\sum_{i=1}^{n} \left(\bar{\mathbf{r}}_i(0) \times \tilde{\mathbf{n}}_i^0(1) \right) = \mathbf{0},$$

where $\tilde{\mathbf{n}}_i^0(1)$ is the approximate static axial force vector of the ith cable calculated at $\sigma = 1$, while $\tilde{\mathbf{H}}^0(\sigma)$ is the diagonal matrix of the unbalanced residual of the equilibrium equations. In particular, the vector of the ith unbalanced residual reads:

$$\tilde{\boldsymbol{\eta}}_i^0(\sigma) = \frac{\kappa_i}{\Lambda_{0,i}^2\, \lambda_{0,i}^4} \left[\frac{(\tilde{\nu}_i^0 - 1)}{\tilde{\nu}_i^0} \tilde{\mathbf{p}}_i^{0\prime} \right]' + \bar{\mathbf{f}}_i, \tag{28}$$

where $\bar{\mathbf{p}}_i^0 = \mathbf{q}_{i,0}^0 \sigma + \sum_{j=1}^m \boldsymbol{\phi}_{i,j}(\sigma)\mathbf{q}_{i,j}^0$ and the trial functions adopted to calculate the approximate solution of the equilibrium problem are the same adopted in the dynamic problem and reported in Eq. (23).

3.2. The case of point mass end-effector

The analytical model formulated in this work includes the most general case of a rigid body end-effector, possessing an orientation and moving in the 3D space. Nevertheless, a further interesting model referring to the case of point mass end-effector can be straightforwardly derived from the equations presented in the previous sections by simply setting to zero the vectors describing the geometry of the end-effector mass, that is $\bar{\mathbf{r}}_i^0 = \mathbf{0}$ $(i = 1, \ldots, n)$. Within this context, it is evident that the rotation angles $\theta_k(\tau)$ $(k = 1, 2, 3)$ of the local frame are no longer necessary to describe the dynamic configuration of the CDPM and so is the balance equation of the angular momentum, i.e., Eq. (26). Therefore, the equations governing the dynamics of the CDPM with point mass end-effector are the equation of motion (24) and the balance Eq. (25) of the linear momentum of the EE, respectively; in particular, the latter reduces to the form

$$\sum_{i=1}^n \tilde{\mathbf{n}}_i(1,\tau) + \mu\,\gamma\,\mathbf{e}_z + \mu\,\ddot{\bar{\mathbf{p}}}_1(1,\tau) = \mathbf{0}, \tag{29}$$

while the trajectory of each point connected to the EE is given by the vector $\bar{\mathbf{p}}_{M,i}(\tau) = \bar{\mathbf{p}}_M(\tau) - \bar{\mathbf{x}}_i$ $(i = 1, \ldots, n)$.

3.3. The reduction to 2D dynamics

Indeed, the here proposed formulation can be easily adapted to study the particular case of the dynamic response constrained in a two-dimensional space. Within this context, all vectors are reduced to a selected plane, for instance (but it is not limited to), the plane $(\mathbf{e}_y, \mathbf{e}_z)$ including the gravity direction, and the dynamics of the system are described by the two-components of the position vector $\bar{\mathbf{p}}_i(\sigma, \tau)$ along the reference axes, i.e., $\bar{p}_{y,i}(\sigma, \tau)$ and $\bar{p}_{z,i}(\sigma, \tau)$, respectively, and by one rotation angle, i.e., $\theta_1(\tau)$.

4. Direct and inverse approaches to the dynamic problems

To discuss in detail the solution strategy adopted to solve the equations of motion of the CDPM with respect to all considered configurations, it is worth to refer to further parameters allowing to classify the system. To this end, the number of system degrees of freedom (DOFs) d is introduced, being $d = d_p + d_\theta$, where d_p and d_θ are the number of translational and rotational DOFs of the end-effector mass, respectively. In Table 1 are reported the number of DOFs for all case-study that can be analyzed by the mechanical model formulated in this paper, that is the 3D and the 2D dynamics of oriented mass and point mass end-effector, respectively.

Table 1
Degrees of freedom of the end-effector in case of 3D and 2D dynamics of oriented mass (OM) and point mass (PM), respectively.

	3D-OM	2D-OM	3D-PM	2D-PM
d_p	3	2	3	2
d_θ	3	1	0	0
d	6	3	3	2

Therefore, the system dynamics are governed by $d_p(nm + 1) + d_\theta$ nonlinear balance equations of linear and angular momentum given by Eqs. (24), (25), and (26), respectively. On the other hand, the dynamic unknowns of the system are the $d_p(nm + 1)$ generalized coordinates collected in the d_p-by-1 vectors $\mathbf{q}_{1,0}(\tau)$ and $\mathbf{q}_{i,j}(\tau)$ $(i = 1, \ldots, n,$ and $j = 1, \ldots, m)$, and the d_θ rotations $\theta_k(\tau)$, $k = 1, \ldots, d_\theta$, respectively.

Nevertheless, the system is characterized by further n unknown functions $\Lambda_i(\tau)$, providing the ratio, at time τ, between the unstretched length $L_i(\tau)$ and the distance $l_i(\tau)$ between the boundaries of the ith cable. These time-dependent parameters play a crucial role in the calculation of the solution of the system equations of motion, and, depending on the solution approach, those can be treated as known, pre-assigned, system parameters or, conversely, unknown functions to be calculated as part of the solution of the dynamic problem, in the direct and in the inverse dynamic approach, respectively.

Moreover, due to the generic number of cables that can be considered in the CDPM model, the latter may result to be under-, over-, or minimally-actuated, respectively. To classify the dynamic system, it is therefore convenient to introduce an additional parameter, namely, the degree of over-actuation o of the CDPM, defined as $o = n - d$. In this work the interest is not devoted to the study of the dynamics of under-actuated CDPM; therefore, by neglecting any possible under-actuated configuration, two scenarios of interest can be considered: namely, the minimally-actuated case, when $o = 0$, and the over-actuated case, when $o > 0$, respectively.

4.1. Direct dynamics

The direct approach consists in assigning *a priori* the values of the n functions $\Lambda_i(\tau)$ and solving the system balance equations in terms of the $d_p(nm+1) + d_\theta$ unknown generalized coordinates and rotations. Unfortunately, this solution approach cannot ensure that the effective motion of the end-effector, together with its orientation, matches exactly the expected trajectory. In fact, within the direct dynamic approach, only the balance equations of linear and angular momentum are verified and no kinematic relationship, providing the exact positioning in space and time of the EE, is satisfied. In particular, the target trajectory of the n connected points of the end-effector given by Eq. (9), is sought by assigning the n functions $\lambda_i(\tau)$ through the nondimensionalized expression of Eq. (10) and solving Eqs. (24), (25), and (26), together with the initial conditions $\mathbf{q}_{1,0}(0) = \mathbf{q}_{1,0}^0$, $\mathbf{q}_{i,j}(0) = \mathbf{q}_{i,j}^0$, $\theta_k(0) = \theta_k^0$, and, $\dot{\mathbf{q}}_{1,0}(0) = \mathbf{0}$, $\dot{\mathbf{q}}_{i,j}(0) = \mathbf{0}$, $\dot{\theta}_k(0) = 0$, which can be calculated by solving Eq. (27).

When solving the equilibrium at the initial time step, the n functions $\lambda_{0,i} = \lambda_i(0)$ $(i = 1, \ldots, n)$ can be calculated through Eq. (10) evaluated at time $\tau = 0$, while an appropriate strategy must be used to calculate the ratios $\Lambda_{0,i} = \Lambda_i(0)$ $(i = 1, \ldots, n)$. To this end, $\Lambda_{0,i}$ can be determined by assuming the cables as massless linear springs and so as to satisfy the equilibrium equations of the end-effector mass as:

$$\sum_{i=1}^n \hat{\mathbf{n}}_i + \mu\,\gamma\,\mathbf{e}_z = \mathbf{0}, \quad \sum_{i=1}^n \left(\bar{\mathbf{r}}_i(0) \times \hat{\mathbf{n}}_i\right) = \mathbf{0}, \tag{30}$$

where $\hat{\mathbf{n}}_i = \kappa_i\left(1 - \Lambda_{0,i}\right)\hat{\mathbf{a}}$ is the vector of the axial force of the ith massless spring directed as the unit vector $\hat{\mathbf{a}} = \bar{\mathbf{p}}_{M,i}(0)/\lambda_{0,i}$ tangent to the distance between the boundary points of the ith cable at $\tau = 0$. Thus, to seek the solution of the direct dynamic problem, the n functions $\Lambda_i(\tau)$ can be assumed constant to the value attained at $\tau = 0$, that is $\Lambda_i(\tau) = \Lambda_{0,i}$. Although, it should be mentioned that Eq. (30) may provide values of $\Lambda_{0,i} \geq 1$ which implies that the ith cable is either stress-free or pre-compressed; such conditions are unrealistic and, in that case, values of $\Lambda_{0,i} < 1$ must be assigned. Moreover, when the system is over-actuated (that is, when $o > 0$) the number of parameters $\Lambda_{0,i}$ is larger than the number of DOF (i.e., $n > d$); therefore, the solution of Eq. (30) depends on o parameters $\Lambda_{0,k}$ $(k = 1, \ldots, o)$ which can be assigned ranging in the positive real number space $\mathbb{R}^+$ considering any value lower than 1.

Finally, it is worth noting that, within the assumptions made to solve the direct problem, the parameters $\Lambda_i(\tau)$ $(i = 1, \ldots, n)$ do not represent, anymore, the effective cables' aspect ratios, since the ith effective distance $l_i(\tau)$ does not coincide with that prescribed through the ith ratio $\lambda_i(\tau)$ and this is the consequence to the non-compatible solution calculated via direct approach.

4.2. Inverse dynamics

The aim of the solution strategy based on the inverse approach is to provide, together with the balance of the linear and angular momentum of the system, also the exact positioning and orientation of the end-effector mass. Within this context, it is a matter of fact that further dynamic compatibility equations must be introduced in the model; therefore, the n functions $\Lambda_i(\tau)$ play the role of further unknowns of the system to be calculated as part of the solution of the direct dynamic problem; moreover, within the inverse approach, the latter represent the effective aspect ratios of the n cables. For the sake of completeness of the discussion, it is worth to point out that the inverse approach, although fascinating from a modeling perspective, does not provide any particular insight in the study of a feasible dynamic response of CDPM. Nevertheless, it may play a fundamental role in the design of model-based and feed-forward control laws since the inverse approach allows to calculate the exact dynamic configurations of the cables (i.e., the stretched and the unstretched lengths, here represented by the parameter $\Lambda_i(\tau)$), or, alternatively, the length-related forces to be provided to each cable during time.

To prescribe the exact trajectory of the EE at time τ, the components of the vector $\mathbf{q}_{1,0}(\tau)$ can be assigned by the relationship

$$\mathbf{q}_{1,0}(\tau) = \bar{\mathbf{p}}_{\mathrm{M}}(\tau) + \Theta(\tau)\,\bar{\mathbf{r}}_1^0, \tag{31}$$

together with the angles $\theta_k(\tau)$ $(k = 1, \ldots, d_\theta)$ which, in turn, become a data of the inverse problem. It is a matter of fact that, within the inverse approach, the d degrees of freedom of the EE mass, given by the d_p components of the vector $\mathbf{q}_{1,0}(\tau)$ and by the d_θ angles $\theta_k(\tau)$, are constrained so as to ensure the exact trajectory of the EE. Therefore, only the $d_p nm$ generalized coordinates $\mathbf{q}_{i,j}(\tau)$ $(i = 1, \ldots, n$, and $j = 1, \ldots, m)$ and the n functions $\Lambda_i(\tau)$ remain to be determined through the $d_p(nm + 1) + d_\theta$ equations of motion.

When the system is minimally actuated (that is, when $n = d = d_p + d_\theta$) the number of equations $d_p(nm + 1) + d_\theta$ turns out to be equal to the number $d_p nm + n$ of the system unknowns; therefore, the solution of the inverse dynamic problem can be calculated. On the other hand, when the system is over actuated (that is, when $n > d = d_p + d_\theta$) the number of equations $d_p(nm + 1) + d_\theta$ is lower than the number $d_p nm + d_p + d_\theta + o$ of unknowns; therefore, the system is over-determined and further equations are needed to calculate a solution. In the latter case, to determine the o unknown parameters $\Lambda_k(\tau)$ $(k = 1, \ldots, o)$ characterizing the over-actuated system, the following o equations, linearly independent from Eqs. (24), (25), and (26), respectively, are considered:

$$\Lambda_{(d+k)}(\tau) = \frac{1}{d} \sum_{h=1}^{d} \Lambda_h(\tau) \quad (k = 1, \ldots, o), \tag{32}$$

which prescribe that the unstretched length-to-span ratios of the o over-actuating cables at time τ are equal to the mean value of the remaining d ratios.

5. Numerical analyses: Application of the model to case-studies CDPMs

In this section, the feasibility of the analytical model developed in the present work is shown by performing numerical simulations on selected CDPM configurations. In particular, the application to the case of 3D dynamics of a point-mass EE is first proposed by analyzing the case-study examined in a recent work published by Du and Agrawal [33], whose geometric and mechanical characteristics are reported below. Differently from the above mentioned work, where the dynamics of the selected CDPM were studied only via a direct approach, in this work it is shown also the solution via the inverse approach. Moreover, the application of the here proposed dynamic model is shown also in the case of a CDPM endowed with an oriented mass EE.

By referring to [33], an EE having mass $M = 20$ kg and connected through $n = 4$ cables is considered in the simulations. The cables are characterized by a mass per unit length $\rho A_i = 4.19 \times 10^{-2}$ kg/m and by an axial stiffness $EA_i = 150.36 \times 10^3$ N $(i = 1, \ldots, n)$; moreover, the dissipative force are neglected, hence, the undamped case, i.e., $\zeta = 0$, is considered. The selected CDPM configuration is depicted in Fig. 2 and the coordinates of the cables' boundaries at $s_i = 0$, provided in the model by the dimensional vector $\mathbf{x}_i$ $(i = 1, \ldots, 4)$, are summarized in Table 2.

Table 2
Coordinates in the fixed frame $(\mathbf{e}_x, \mathbf{e}_y, \mathbf{e}_z)$ of the cables' boundaries at $s_i = 0$. Case-study taken from [33] with $n = 4$ and point mass end-effector, dimensions are in meters (m).

i	1	2	3	4
x_i	0	40	0	40
y_i	0	0	30	30
z_i	0	0	0	0

The end-effector is demanded to track an horizontal, circular, trajectory given by the vector $\mathbf{p}_{\mathrm{M}}(t) = \left[(20 + \Delta_p \cos \Omega t) \;\; (15 + \Delta_p \sin \Omega t) \;\; -5 \right]^{\mathsf{T}}$ (components are in meters), where $\Delta_p = 2.5$ m and the angular velocity of the prescribed motion is assumed to be $\Omega = 0.314$ rad/s; therefore, the overall motion lasts 20 s; finally, at time $t = 0$ the position in space of the end-effector is given by the vector $\mathbf{p}_{\mathrm{M}}(0) = [22.5 \;\; 15 \;\; -5]^{\mathsf{T}}$.

As mentioned before, further analyses are also carried out to validate the fully 3D dynamic model of CDPM considering the case of rigid-body end-effector and its orientation in space. The mechanic characteristics of the cables are kept identical to those used in the point-mass EE case-study, including the weight of the EE mass. On the other hand, although the geometry of the end-effector can be generic, in the present case-study a square cuboid, having height of 1 m and the two square faces having edges length of 0.5 m, is considered. Therefore, the dimensional vectors describing the geometry of the end-effector mass are (dimensions are in meters): $\mathbf{r}_1^0 = [-0.25 \;\; -0.25 \;\; 0.5]^{\mathsf{T}}$, $\mathbf{r}_2^0 = [0.25 \;\; -0.25 \;\; 0.5]^{\mathsf{T}}$, $\mathbf{r}_3^0 = [0.25 \;\; 0.25 \;\; 0.5]^{\mathsf{T}}$, $\mathbf{r}_4^0 = [-0.25 \;\; 0.25 \;\; 0.5]^{\mathsf{T}}$, $\mathbf{r}_5^0 = [-0.25 \;\; -0.25 \;\; -0.5]^{\mathsf{T}}$, $\mathbf{r}_6^0 = [0.25 \;\; -0.25 \;\; -0.5]^{\mathsf{T}}$, $\mathbf{r}_7^0 = [0.25 \;\; 0.25 \;\; -0.5]^{\mathsf{T}}$, $\mathbf{r}_8^0 = [-0.25 \;\; 0.25 \;\; -0.5]^{\mathsf{T}}$, respectively. Finally, the matrix of the principal mass moment of inertia with respect to the local frame $\left(\mathbf{b}_1(t), \mathbf{b}_2(t), \mathbf{b}_3(t) \right)$ is given by

$$\mathbf{J}_{\mathrm{M}} = M \begin{bmatrix} 0.1042 & 0 & 0 \\ 0 & 0.1042 & 0 \\ 0 & 0 & 0.0417 \end{bmatrix} \mathrm{kg\,m^2}. \tag{33}$$

Moreover, in the present case-study also small damping effects are considered by assuming in the simulations a damping ratio $\zeta = 0.5\%$ for each cable. Finally, the selected CDPM configuration is depicted in Fig. 3 and the coordinates of the cables' boundaries at $s_i = 0$, provided in the model by the dimensional vector $\mathbf{x}_i$ $(i = 1, \ldots, 8)$, are summarized in Table 3.

Table 3
Coordinates in the fixed frame $(\mathbf{e}_x, \mathbf{e}_y, \mathbf{e}_z)$ of the $n = 8$ cables' boundaries at $s_i = 0$, with oriented mass end-effector, dimensions are in meters (m).

i	1	2	3	4	5	6	7	8
x_i	0	40	40	0	0	40	40	0
y_i	0	0	30	30	0	0	30	30
z_i	0	0	0	0	−10	−10	−10	−10

A horizontal, circular, trajectory of the EE center of mass, given by the vector $\mathbf{p}_{\mathrm{M}}(t) = \left[(20 + \Delta_p \cos \Omega t) \;\; (15 + \Delta_p \sin \Omega t) \;\; -5 \right]^{\mathsf{T}}$ (components are in meters and $\Delta_p = 2.5$ m), is prescribed together with the constraint that no proper rotations of the EE are allowed, i.e., $\Theta(t) = \mathbf{O}$. Moreover, an angular velocity equal to $\Omega = 0.314$ rad/s is considered.

Finally, it is worth mentioning that, for all simulations performed in this work, results were reported in dimensional form so as to allow an easier interpretation of the phenomena investigated.
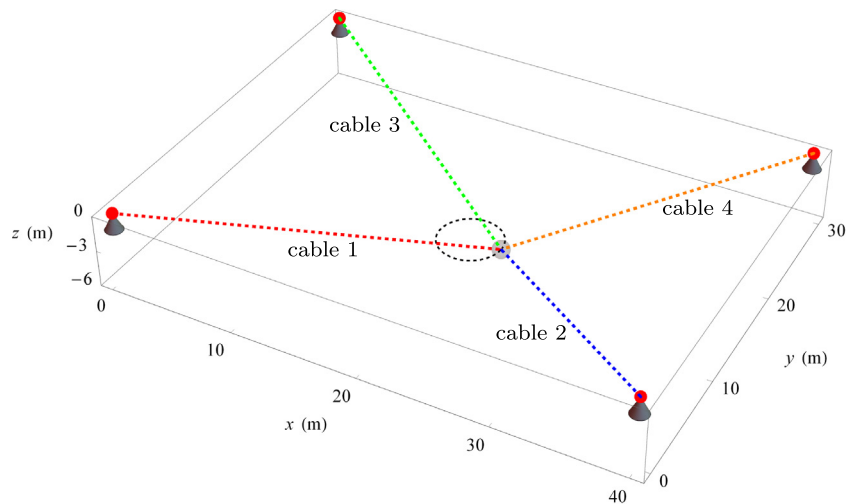
Fig. 2. Configuration of the point-mass EE. Red, blue, green, and orange dashed lines indicate the directions of cables 1, 2, 3, and 4, respectively; while black dashed line represents the EE trajectory. (For interpretation of the references to color in this figure legend, the reader is referred to the web version of this article.)
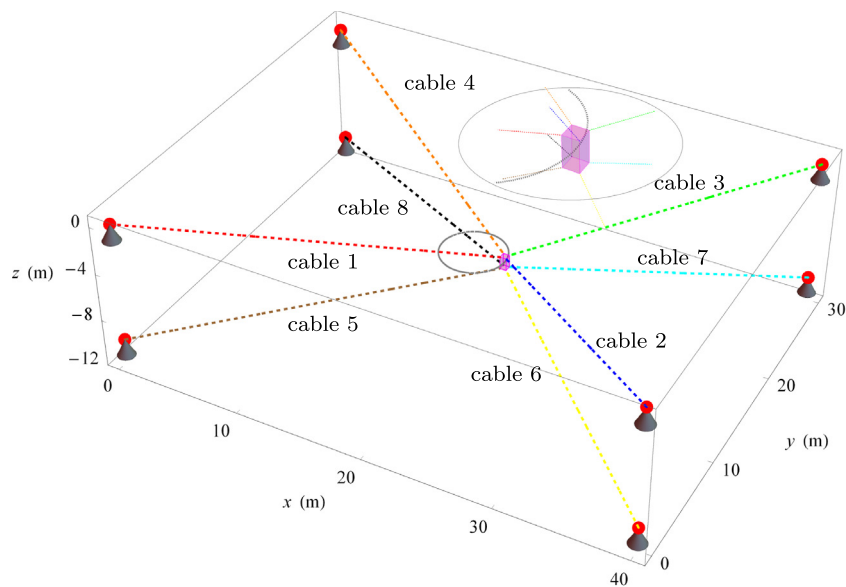

Fig. 3. Configuration of the oriented mass EE. Red, blue, green, orange, brown, yellow, cyan, and black dashed lines indicate the directions of cables 1, 2, 3, 4, 5, 6, 7 and 8, respectively; while gray dashed line represents the EE trajectory. The inset shows a zoomed view of the three-dimensional EE. (For interpretation of the references to color in this figure legend, the reader is referred to the web version of this article.)

5.1. Direct dynamics simulations for point-mass EE

Simulations were performed by considering 5 trial functions (i.e., $m = 4$) to approximate the solution vector of each cable and the numerical computations were carried by implementing an in-house made code in the software Mathematica© [49].

The case-study investigated was representative of an over-actuated system with degree of over actuation $o = 1$. As discussed in the last part of Section 4.1, tentative values of the ratios $\Lambda_{0,i}$ ($i = 1, \ldots, 4$) can be calculated according to the relationship given by Eq. (30) and the indeterminacy of the oth ratio was resolved by borrowing Eq. (32) so as to obtain the following set of values: $\Lambda_{0,1} = 0.998373$, $\Lambda_{0,2} = 0.998708$, $\Lambda_{0,3} = 0.999157$, $\Lambda_{0,4} = 0.997255$. Hence, the equilibrium configuration at $t = 0$ was first calculated in order to describe the state of the CDPM representative, together with the assumption of zero velocity, of the initial condition necessary to solve the equations of motion of the system. In Fig. 4(a) and (b), is shown the equilibrium configuration of the CDPM and a zoomed view of the EE neighborhood, respectively, and colored lines represent the four elastic cables. On the other hand,

straight, dashed lines represent the distance between the cable boundaries at $t = 0$, while the dotted circular line is the considered trajectory. As discussed in Section 4.1, within the context of the direct dynamic approach the exact position of the EE cannot be granted; in fact, in the case-study here investigated, the equilibrium of the EE at time $t = 0$ was reached at the position $\mathbf{p}^*_M(0) = [22.5097 \ 15.0095 \ -5.01324]^\top$, which corresponds to an error with respect to the assigned position $\mathbf{p}_M(0)$ of 0.04%, 0.06%, and 0.265%, in the components along $\mathbf{e}_x$, $\mathbf{e}_y$, and $\mathbf{e}_z$, respectively. Finally, Fig. 4(c) and (d) depict the stress state of cables 1 and 4 and of cables 2 and 3, respectively, showing the variation of the axial force along the arclength s_i of the corresponding cable, whose total length $L_i(0)$ was not the same for all cables due to the non-symmetric position of the EE mass at $t = 0$.

In Fig. 5 the black solid lines represent the motion of the EE mass simulated via direct approach in terms of the component along $\mathbf{e}_x$, $\mathbf{e}_y$, and $\mathbf{e}_z$, of the position vector of cable 1 at $s_1 = L_1(t)$ (i.e., the connection of cable 1 with the EE), respectively shown in Fig. 5(a), (b), and (c). The effective motion was compared with the ideal trajectory represented by the red dashed lines. As expected, the motion of the
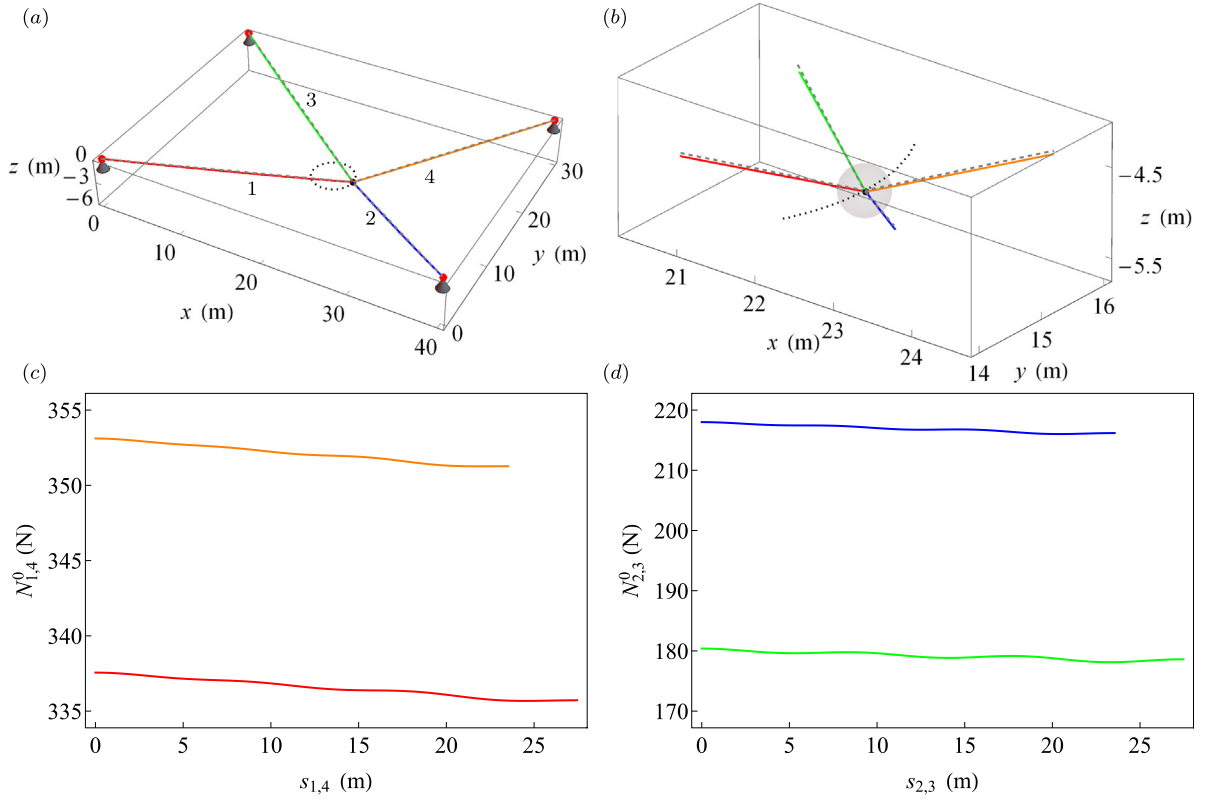
Fig. 4. Equilibrium configuration of the point-mass EE along the selected trajectory at $t = 0$ (a), and close-up of the end-effector position (b). Axial forces in cables 1 and 4 (c) and in cables 2 and 3 (d) along the corresponding unstretched, dimensional, arclength s_i. Red, blue, green, and orange colors indicate cables 1, 2, 3, and 4, respectively. (For interpretation of the references to color in this figure legend, the reader is referred to the web version of this article.)
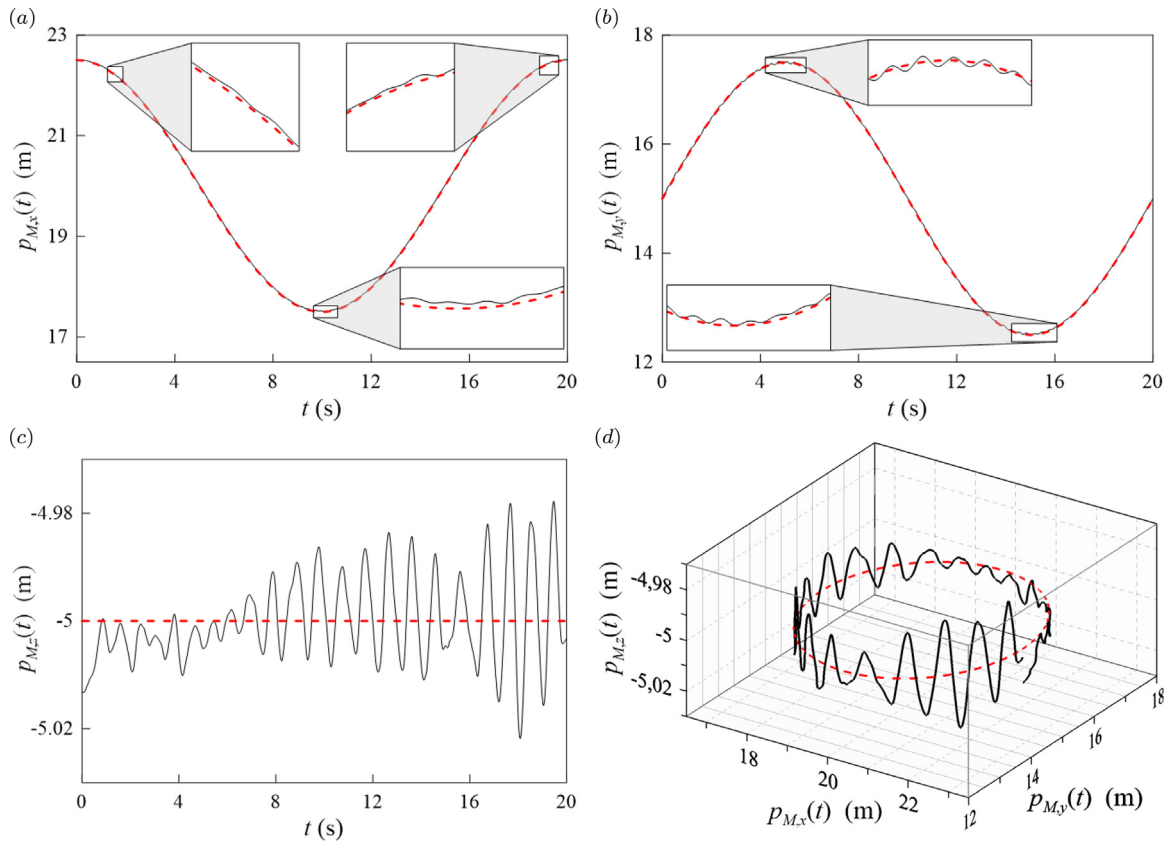

Fig. 5. Time history of the point-mass EE motion for a selected trajectory in terms of the position vector $\mathbf{p}_M(t)$: (a) component along the global direction $\mathbf{e}_x$, (b) component along the global direction $\mathbf{e}_y$, (c) component along the global direction $\mathbf{e}_z$, and (d) 3D motion.
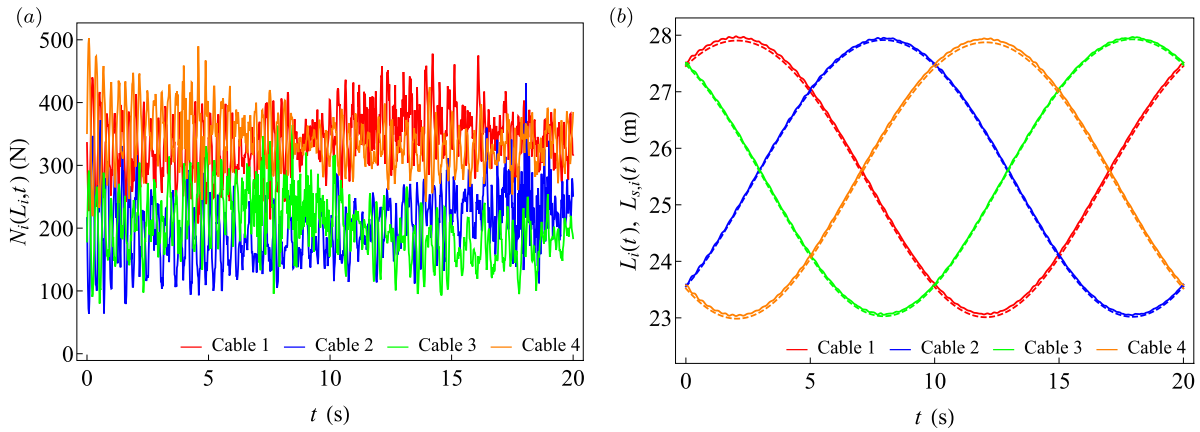
Fig. 6. (a) time variation of the cables' axial forces at $s_i = L_i(t)$, and (b) unstretched length $L_i(t)$ (solid lines) versus stretched length $L_{s,i}(t)$ (dashed lines) for $i = 1, \ldots, 4$. Red, blue, green, and orange colors indicate cables 1, 2, 3, and 4, respectively. (For interpretation of the references to color in this figure legend, the reader is referred to the web version of this article.)
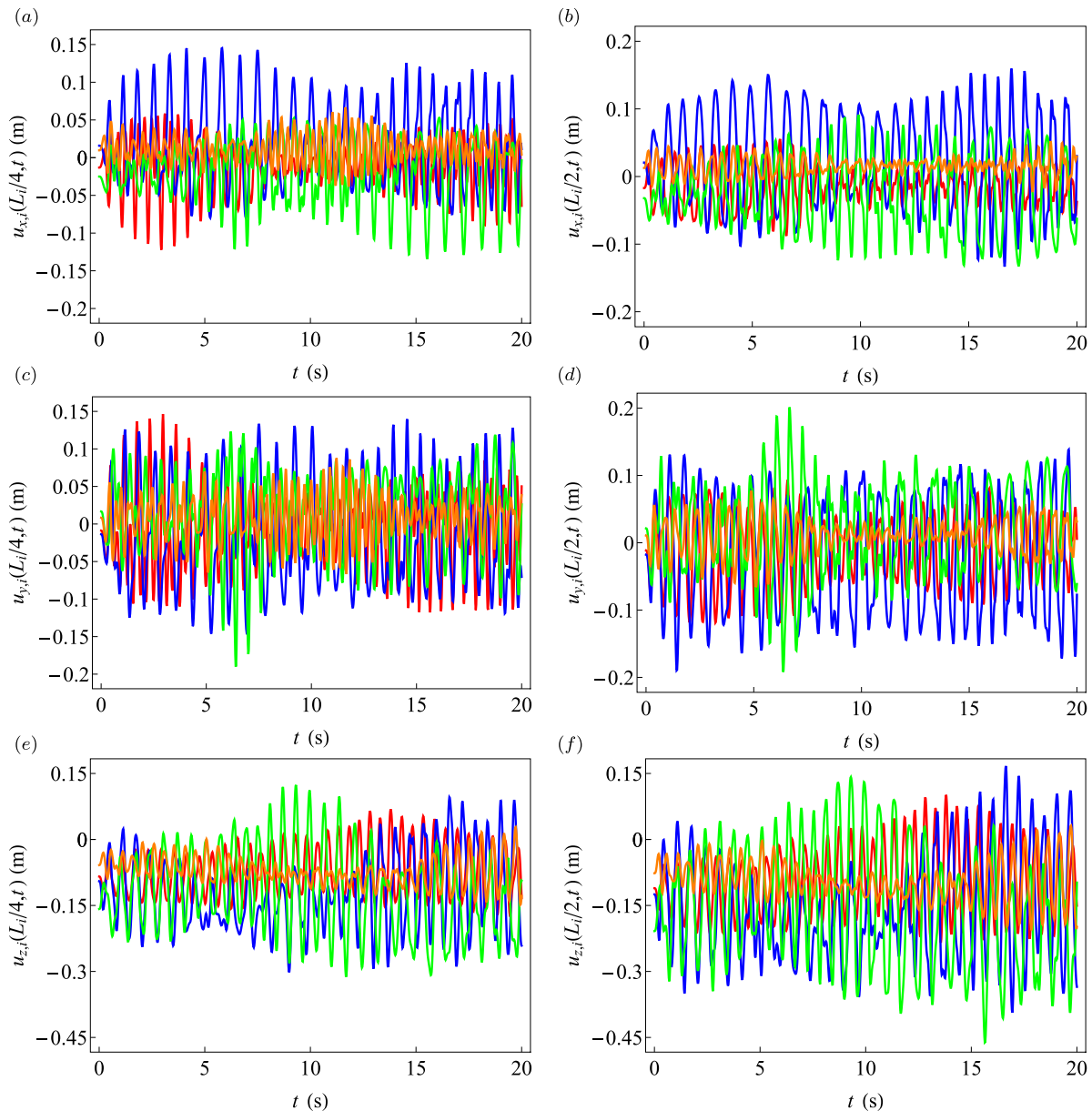
Fig. 7. Components, at time t, along the axis $\mathbf{e}_x$, $\mathbf{e}_y$, and $\mathbf{e}_z$ of the position vector of: (a), (c), and (e), the quarter-span point, and (b), (d), and (f), the mid-span point of the four cables. Red, blue, green, and orange colors indicate cables 1, 2, 3, and 4, respectively. (For interpretation of the references to color in this figure legend, the reader is referred to the web version of this article.)
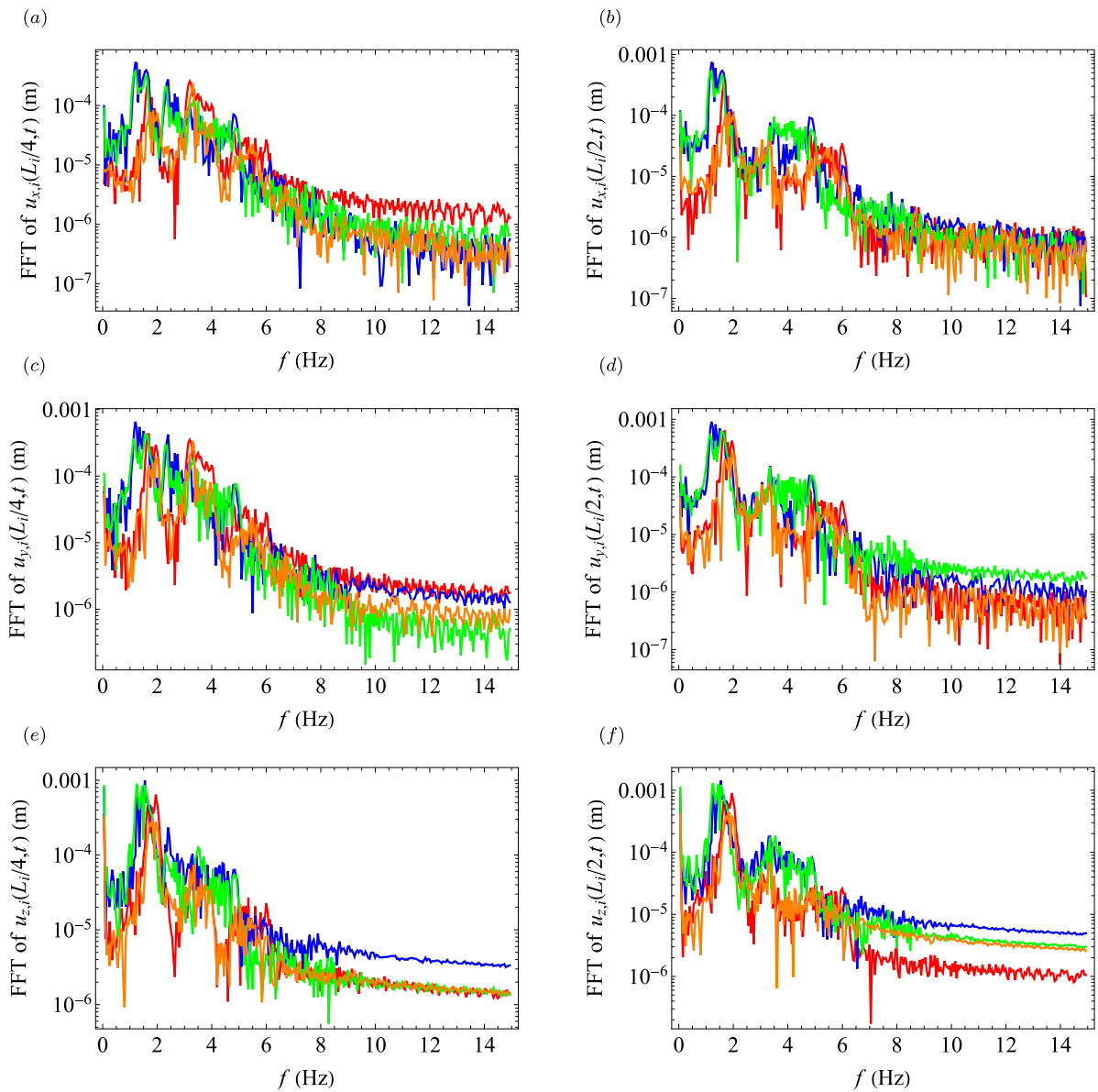
Fig. 8. Fast Fourier Transform (FFT) of the components, along the axis $\mathbf{e}_x$, $\mathbf{e}_y$, and $\mathbf{e}_z$ of the position vector of: (a), (c), and (e), the quarter-span point, and (b), (d), and (f), the mid-span point of the four cables. Red, blue, green, and orange colors indicate cables 1, 2, 3, and 4, respectively. (For interpretation of the references to color in this figure legend, the reader is referred to the web version of this article.)

end-effector shows oscillations near the ideal trajectory and this is due to the choice to keep constant in time the ratios $\Lambda_i(t)$ ($i = 1, \ldots, 4$) by assuming those equal to the corresponding values $\Lambda_{0,i}$, calculated as discussed in the previous paragraph.

The parametric model developed in this work allowed also to recover the time histories of the axial forces along the cables' arclength and to monitor the change in time of cables' length. Such results are shown in Fig. 6 where are reported, at time t, the axial forces at $s_i = L_i(t)$ (i.e., at the connection with the end-effector) and the time histories of the total stretched and unstretched lengths of the four cables, in Fig. 6(a) and (b), respectively. In particular, in the case-study investigated, cable 1 (red lines) and cable 4 (orange lines) possess almost twice the tension of cable 2 (blue lines) and cable 3 (green lines), respectively, even though their total length varies in the same range. This is due only to the choice of fixing in time the ratios $\Lambda_i(t)$ at selected values approximately calculated as discussed in the previous section.

The time histories of the dynamic response of the four cables are shown in Fig. 7 in terms of the components along $\mathbf{e}_x$, $\mathbf{e}_y$, and $\mathbf{e}_z$ of

the displacement vector $\mathbf{u}_i(s_i, t)$ (i.e., the displacement with respect to the straight line connecting the two boundaries of each cable) of the quarter-span point of the cables, i.e., Fig. 7(a), (c), (e), and of the mid-span point, i.e., Fig. 7(b), (d), (f). The maximum displacement in the horizontal plane ($\mathbf{e}_x$, $\mathbf{e}_y$) is, on average, around the 0.6% and the 0.8% of the corresponding length $L_i(t)$ for the quarter-span and for the mid-span points, respectively; on the other hand, along the vertical direction $\mathbf{e}_z$ the displacements are, on average, around the 1.2% and the 1.8% of the corresponding length $L_i(t)$, respectively. The Fast Fourier Transforms (FFT) of the above-mentioned time histories are reported in Fig. 8 which shows the rich content in frequency of the response. On the other hand, the shape of the components of vector $\mathbf{u}_i(s_i, t)$ along the arclength of the four cables are depicted in Fig. 9 for selected time instants; in the figure can be appreciated the contribution of the four sinusoidal trial functions adopted in the discretization. The figure shows that for taut cables, i.e., cable 1 (red lines) and cable 4 (orange lines), the shape of the cable motion is mainly characterized by the lowest two sinusoidal functions adopted to approximate the solution (i.e., $j = 1, 2$ in Eq. (20)) while in slack cables, i.e., cable 2 (blue lines) and cable
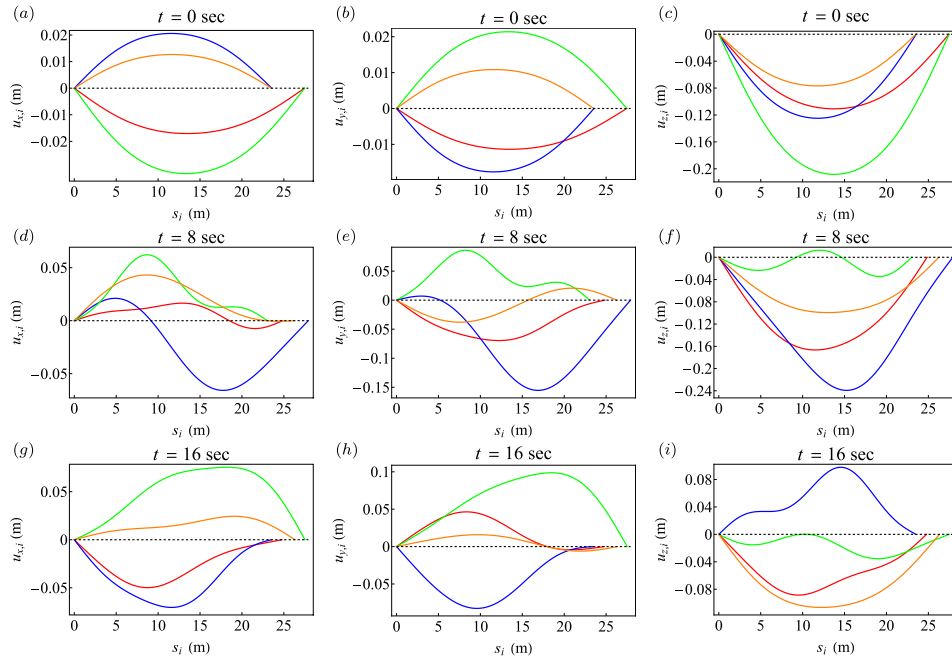
Fig. 9. Dynamic displacements of the four cables at selected times. Displacements along the $\mathbf{e}_x$ direction (a), (d), and (g), displacements along the $\mathbf{e}_y$ direction (b), (e), and (h), and displacements along the $\mathbf{e}_z$ direction (c), (f), and (i). Red, blue, green, and orange colors indicate cables 1, 2, 3, and 4, respectively. (For interpretation of the references to color in this figure legend, the reader is referred to the web version of this article.)
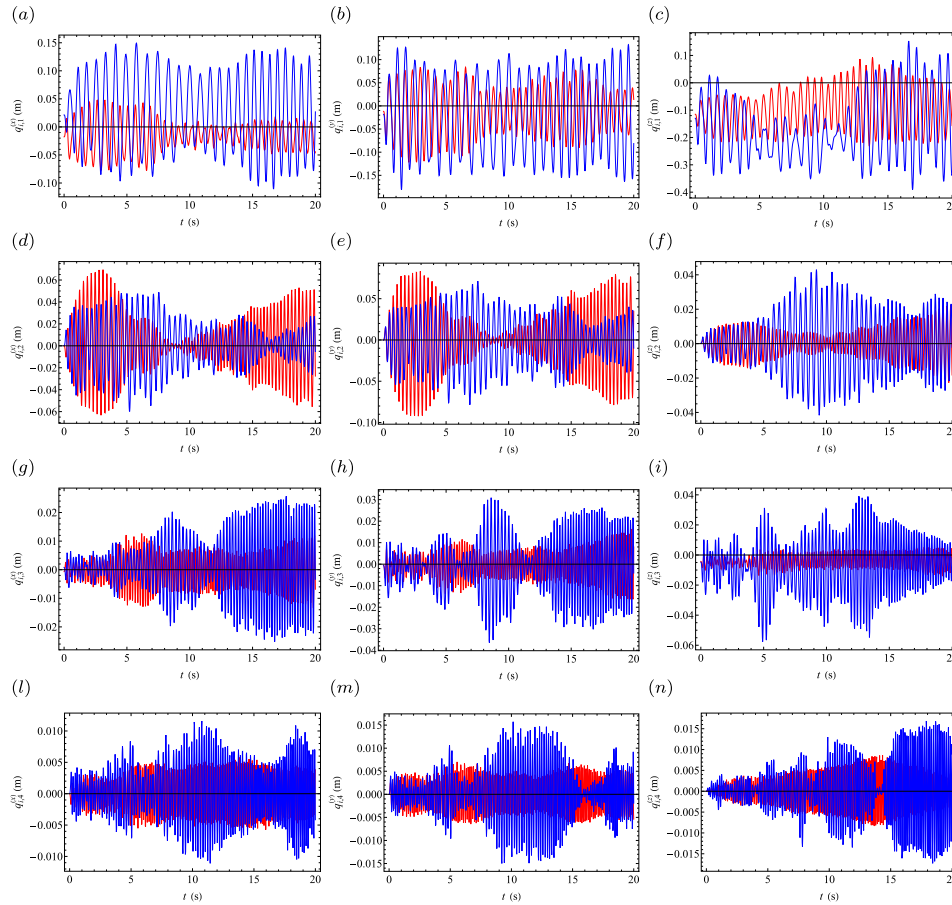

Fig. 10. Time history of the unknown generalized coordinates of cable 1 (red lines, $i = 1$) and cable 2 (blue lines, $i = 2$): plots (a), (d), (g), and (l) show the components $q_{i,1}^{(x)}$, $q_{i,2}^{(x)}$, $q_{i,3}^{(x)}$, and $q_{i,4}^{(x)}$, respectively; plots (b), (e), (h), and (m) show the components $q_{i,1}^{(y)}$, $q_{i,2}^{(y)}$, $q_{i,3}^{(y)}$, and $q_{i,4}^{(y)}$, respectively; plots (c), (f), (i), and (n) show the components $q_{i,1}^{(z)}$, $q_{i,2}^{(z)}$, $q_{i,3}^{(z)}$, and $q_{i,4}^{(z)}$, respectively. (For interpretation of the references to color in this figure legend, the reader is referred to the web version of this article.)
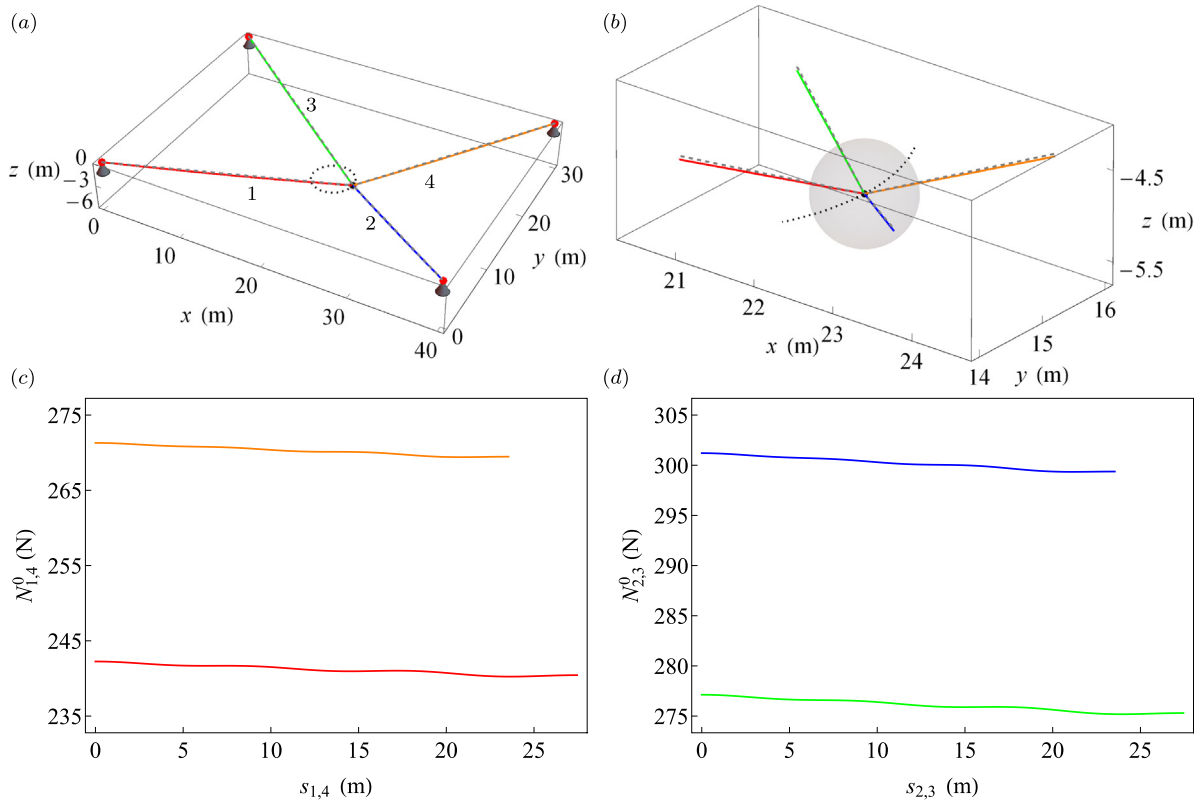
Fig. 11. Inverse approach, equilibrium configuration of the point-mass EE along the selected trajectory at $t = 0$ (a), and close-up of the end-effector position (b). Axial forces in cables 1 and 4 (c) and in cables 2 and 3 (d) along the corresponding unstretched, dimensional, arclength s_i. Red, blue, green, and orange colors indicate cables 1, 2, 3, and 4, respectively. (For interpretation of the references to color in this figure legend, the reader is referred to the web version of this article.)

3 (green lines), also the third and the fourth sinusoidal components (i.e., $j = 3, 4$) are representative of the cable dynamics. This is, in fact, corroborated by the results shown in Fig. 10 where are reported the dynamics of the generalized coordinates corresponding to the lowest four sinusoidal trial functions adopted to discretize the position of cable 1 and cable 2, respectively. In particular, it is evident that in cable 2, oscillating at lower tension level, as shown in Fig. 6(a), the third and the fourth generalized coordinates reach non-negligible amplitudes with respect to the first and second generalized coordinates. Hence, the study conducted highlighted the importance of the discretization order of the solution of the CDPM equations of motion depending on the stress level possessed by the cables during the entire motion.

5.2. Inverse dynamics simulations for point-mass EE

In this section, the dynamic response of the over-actuated CDPM endowed with point-mass EE was studied by solving the equations of motion according to the approach based on the inverse dynamics. The motion of the system was therefore described correctly both in terms of balance of linear and angular momentum and in terms of exact trajectory followed by the EE. The solution of the inverse dynamic problem, in fact, provided the time evolution of the aspect ratios $\Lambda_i(t)$ necessary to seek the assigned trajectory of the EE. Five trial functions (i.e, $m = 4$) were considered also in the present case-study and the solution of the equilibrium at time $t = 0$ was determined so as to provide the initial conditions of the CDPM motion. In particular, as per the analyses conducted in the previous section, due to the non-symmetric position of the EE mass at $t = 0$, the initial length $L_i(0)$ was not the same for the four cables. The results in terms of equilibrium configuration and axial forces along the cables' dimensional arclength s_i are reported in Fig. 11. Differently from the direct approach, the four parameters $\Lambda_{0,i} = \Lambda_i(0)$ are, indeed, solutions of the inverse dynamic problem and represent the aspect ratios that the four cables
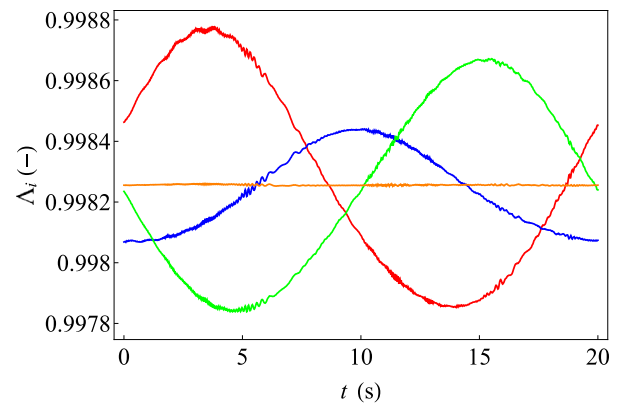

Fig. 12. Inverse approach, time histories of the aspect ratios $\Lambda_i(t)$ ($i = 1, \ldots, 4$). Red, blue, green, and orange colors indicate cables 1, 2, 3, and 4, respectively. (For interpretation of the references to color in this figure legend, the reader is referred to the web version of this article.)

must possess in order to reach the exact position in space of the EE. The values of the aspect ratios, solution of the inverse problem, are reported in Table 4 and are compared with the approximate values assigned in the direct problem. The table shows also the percentage differences of the parameters between the inverse and the direct approaches, respectively; although very small, the differences in the aspect ratios of the cables are such to provide largely different values of the cables' axial forces between the two approaches.

Similarly to the equilibrium problem, the inverse approach allows also to calculate a balanced and compatible solution of the equations of motion; therefore, ensuring that the motion of the EE follows exactly the assigned trajectory. This is due to the fact that, while in the direct
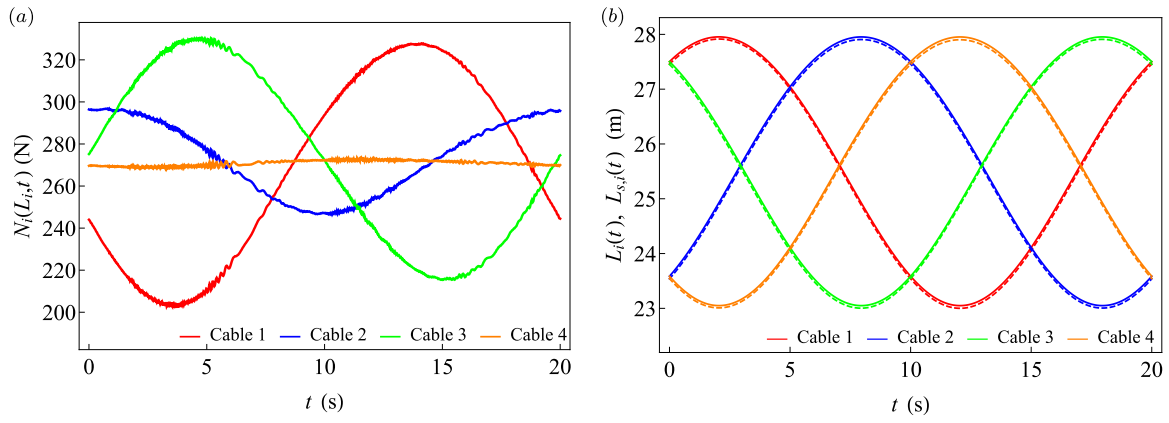
Fig. 13. Inverse approach, (a) time variation of the cables' axial forces at $s_i = L_i(t)$, and (b) unstretched length $L_i(t)$ (solid lines) versus stretched length $L_{s,i}(t)$ (dashed lines), for $i = 1, \ldots, 4$. Red, blue, green, and orange colors indicate cables 1, 2, 3, and 4, respectively. (For interpretation of the references to color in this figure legend, the reader is referred to the web version of this article.)
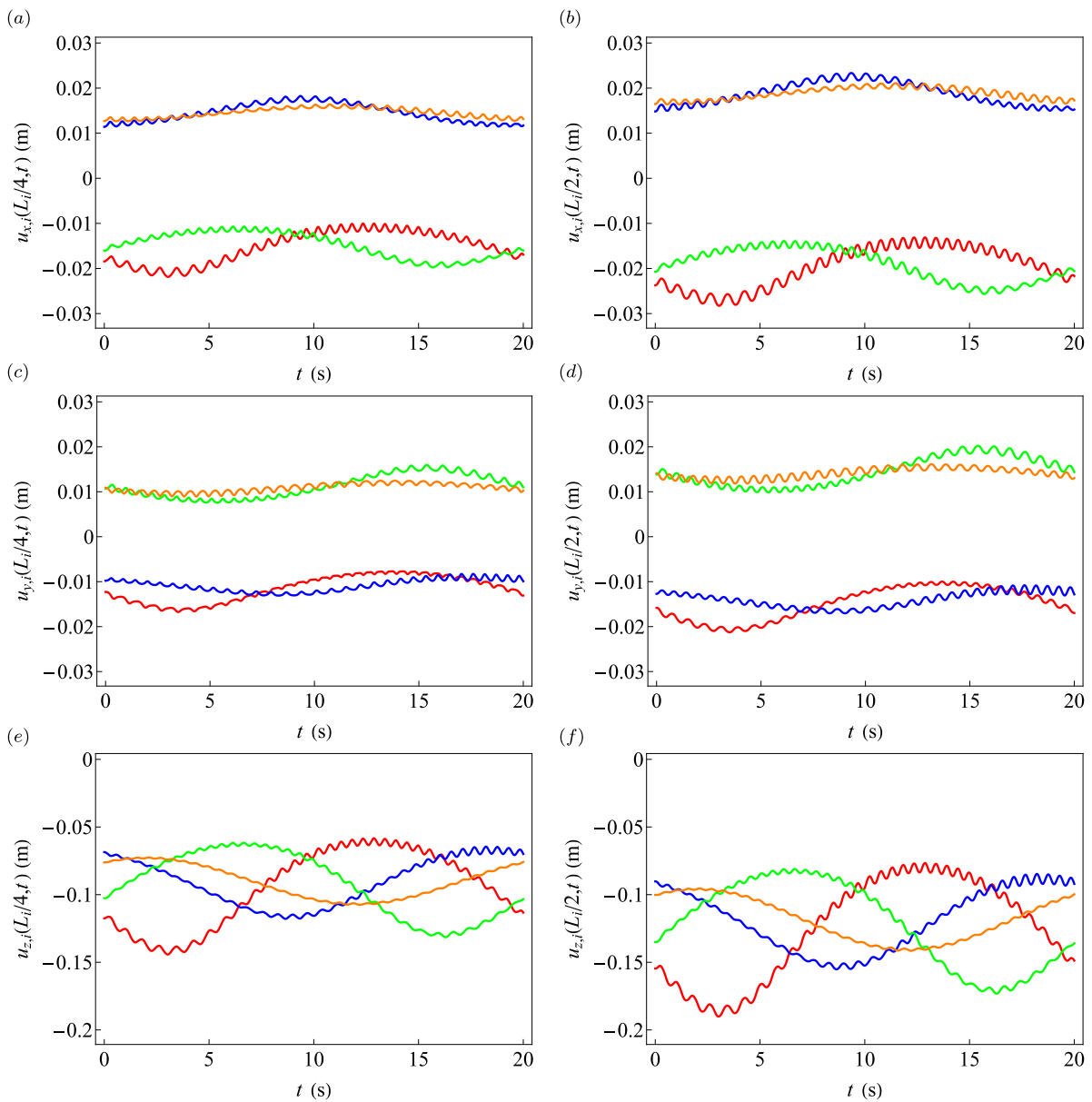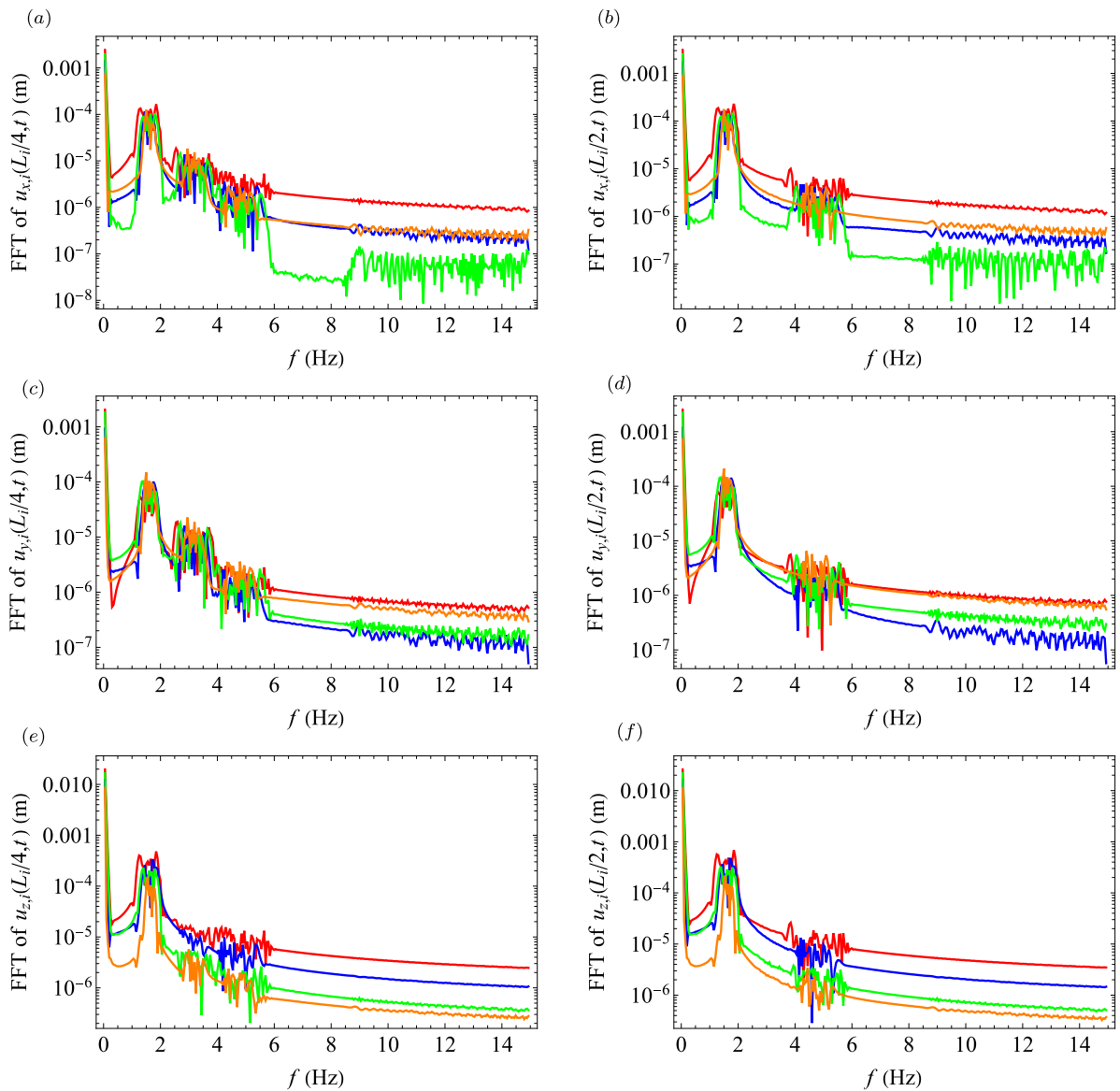

Fig. 14. Inverse approach, components, at time t, along the axis $\mathbf{e}_x$, $\mathbf{e}_y$, and $\mathbf{e}_z$ of the position vector of: (a), (c), and (e), the quarter-span point, and (b), (d), and (f), the mid-span point of the four cables. Red, blue, green, and orange colors indicate cables 1, 2, 3, and 4, respectively. (For interpretation of the references to color in this figure legend, the reader is referred to the web version of this article.)

Fig. 15. Inverse approach, Fast Fourier Transform (FFT) of the components along the axis $\mathbf{e}_x$, $\mathbf{e}_y$, and $\mathbf{e}_z$ of the position vector of: (a), (c), and (e), the quarter-span point, and (b), (d), and (f), the mid-span point of the four cables. Red, blue, green, and orange colors indicate cables 1, 2, 3, and 4, respectively. (For interpretation of the references to color in this figure legend, the reader is referred to the web version of this article.)

Table 4
Values of the aspect ratio $\Lambda_{0,i}$ in the direct and inverse problem and percentage difference for the case-study CDPM with point-mass EE and $n = 4$ cables.

	i	1	2	3	4
Direct	Λ_{0_i}	0.998470	0.998049	0.998234	0.998257
Inverse	Λ_{0_i}	0.998373	0.998708	0.999157	0.997255
Difference		−0.0097%	0.066%	0.0925%	−0.1%

approach the aspect ratios are assigned by tentative values and are then assumed to be constant in time, in the inverse dynamic problem those are solution of the equations of motion and vary in time, as shown in Fig. 12, so as to ensure the match between the effective motion of the EE and the assigned trajectory. In particular, in the simulations the aspect ratios of cables 1, 2, and 3 (red, blue, and green lines, respectively) varied significantly in time, while that of cable 4 (orange line) turned out to be almost constant during the overall motion and this was due to the fact that the aspect ratio of cable 4 was constrained to satisfy Eq. (32).

The time histories of the axial forces at $s_i = L_i(t)$ (i.e., at the connection with the end-effector) and the variation in time of the cables stretched and unstretched lengths are shown in Fig. 13(a) and (b), respectively. Differently from the results obtained via the direct approach, the solution of the inverse dynamic problem showed, for the case-study investigated, that cable 1 (red lines) and cable 3 (green lines) had a larger range of variation of the maximum and minimum axial tension with respect to cable 2 (blue lines) and cable 4 (orange lines); the latter, accordingly with the constraint given by Eq. (32), showed an almost average value of the axial force in the whole dynamic response.

Finally, the time histories of the cables' displacements along $\mathbf{e}_x$, $\mathbf{e}_y$, and $\mathbf{e}_z$ are shown in Fig. 14; in particular, the motions of the quarter-span points with respect to the straight line connecting the two boundaries of the cable, are reported in Fig. 14(a) (c) (e), while those of the mid-span points are shown in Fig. 14(b) (d) (f). It is evident that the solution of the inverse problem provides a more regular dynamic response of all cables characterized by a main content in frequency coming from the contribution of lowest trial functions approximating the solution. In particular, two main frequencies appear
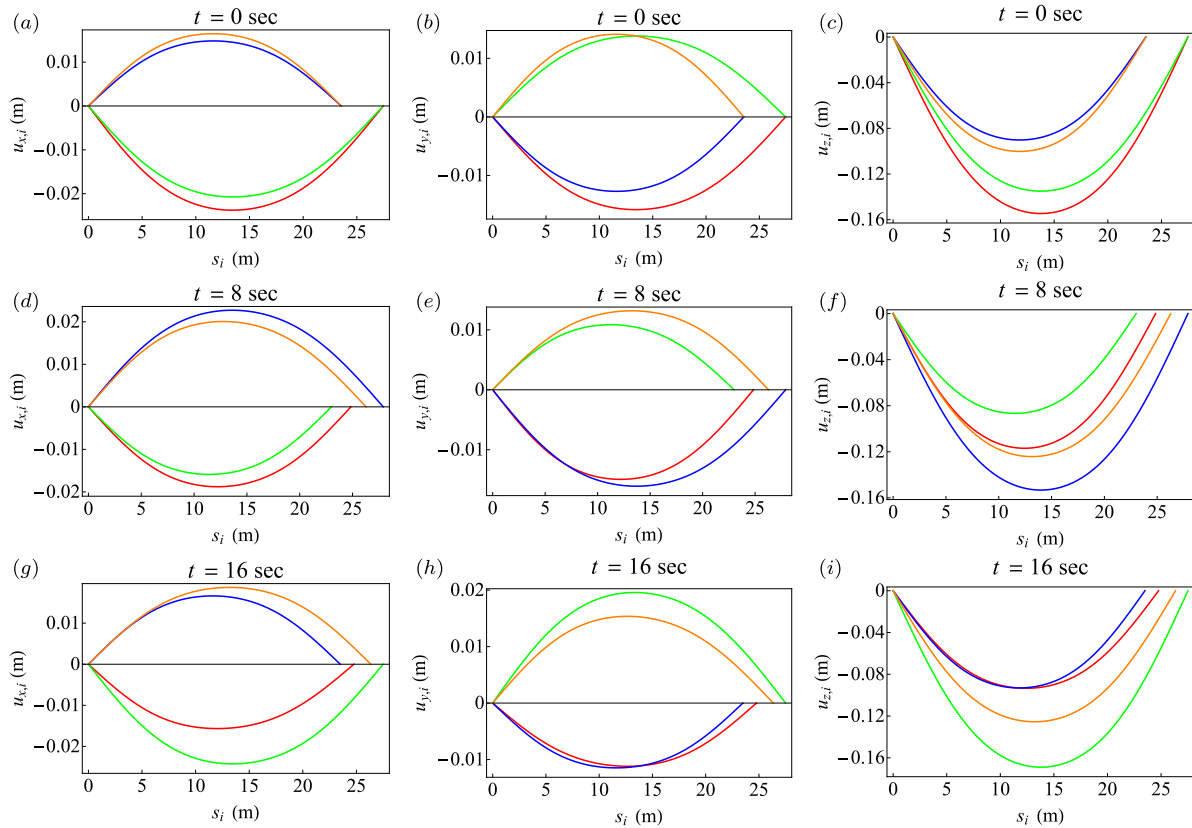
Fig. 16. Inverse approach, dynamic displacements of the four cables at selected times. Displacements along the $\mathbf{e}_x$ direction (a), (d), and (g), displacements along the $\mathbf{e}_y$ direction (b), (e), and (h), and displacements along the $\mathbf{e}_z$ direction (c), (f), and (i). Red, blue, green, and orange colors indicate cables 1, 2, 3, and 4, respectively. (For interpretation of the references to color in this figure legend, the reader is referred to the web version of this article.)

to characterized the dynamic response of the cables, namely, that of the prescribed circular trajectory (i.e., $\Omega/2\pi$, which corresponds to the lowest frequency of the response $f = 0.05$ Hz), and that of the lowest trial function adopted in the discretization (i.e., $j = 1$, $f \approx 1.9$ Hz), as shown in Fig. 15, where are reported the FFT of the cables' displacements along the directions $\mathbf{e}_x$, $\mathbf{e}_y$, and $\mathbf{e}_z$, respectively. This is verified also by the results shown in Fig. 16, where the configurations of the four cables are displayed for selected times. In this figure, only the contribution of the lowest sinusoidal trial function (i.e., $j = 1$) appears to be relevant. This is, in fact, further confirmed by the results shown in Fig. 17 where are reported the time histories of the generalized coordinates corresponding to the lowest four sinusoidal trial functions used to discretize the position of cable 1. The figure clearly shows that trial functions corresponding to $j \geq 2$ provide a negligible contribution to the dynamic response of the cables, being the corresponding generalized coordinates $q_{1,j}^{(x)}$, $q_{1,j}^{(y)}$, and $q_{1,j}^{(z)}$ $(j = 2, 3, 4)$, order of magnitude lower that $q_{1,1}^{(x)}$, $q_{1,1}^{(y)}$, and $q_{1,1}^{(z)}$, respectively.

Hence, the study conducted highlighted the fact that the effective dynamics of the CDPM, whose full description can be obtained by an inverse approach, can be studied by adopting a low order discretization (a single sinusoidal trial function is needed), and so by strongly reducing the computational effort, in contrast to the direct approach for which a higher order discretization is required.

5.3. Direct dynamics simulations for EE with oriented mass

In this section, the motion of a three-dimensional end-effector over-actuated by means of eight cables (i.e., degree of over actuation $o = 2$) is investigated by adopting the direct dynamic approach to show the feasibility of the analytical model developed in this work to properly

describe the 3D dynamics of a CDPM. Tentative values of the ratios $\Lambda_{0,i}$ $(i = 1, \ldots, 8)$ were calculated according to the relationship given by Eq. (30) and the indeterminacy of the oth ratio was resolved by borrowing Eq. (32) so as to obtain the following set of values: $\Lambda_{0,1} = 0.994175$, $\Lambda_{0,2} = 0.994175$, $\Lambda_{0,3} = 0.989284$, $\Lambda_{0,4} = 0.996243$, $\Lambda_{0,5} = 0.999$, $\Lambda_{0,6} = 0.988343$, $\Lambda_{0,7} = 0.999133$, $\Lambda_{0,8} = 0.989526$. Hence, in Fig. 18(a) and (b), is shown the equilibrium configuration of the CDPM and a zoomed view of the 3D end-effector, respectively, and colored lines represent the eight elastic cables. On the other hand, straight, dashed lines represent the distance between the cable boundaries at $t = 0$. As discussed before, within the context of the direct dynamic approach the exact position and orientation of the EE cannot be obtained; therefore, in the case-study here investigated, the equilibrium of the EE at time $t = 0$ was reached at the position of its center of mass $\mathbf{p}^*_{\mathrm{M}}(0) = [22.5211\ 15.0005\ -5.10016]^\top$, which corresponds to an error with respect to the assigned position $\mathbf{p}_{\mathrm{M}}(0)$ of 0.09%, 0.003%, and 2.003%, in the components along $\mathbf{e}_x$, $\mathbf{e}_y$, and $\mathbf{e}_z$, respectively. Furthermore, the EE orientation was calculated to be described by the non trivial angles $\theta_1^0 = -3.01$ deg, $\theta_2^0 = 2.61$ deg, and $\theta_3^0 = 1.98$ deg, despite the assigned trajectory considered zero rotations. Finally, Fig. 18(c) and (d) depict the stress state of cables 2, 4, 5, and 7, and of cables 1, 3, 6, and 8, respectively, showing the variation of the axial force along the arclength s_i of the corresponding cable, whose total length $L_i(0)$ was not the same for all cables due to the non-symmetric position of the EE mass at $t = 0$.

In Fig. 19 are shown the time histories of the axial forces at the connection of each cable to the end-effector together with the variation in time of the stretched and unstretched lengths of the cables, respectively. In particular, in the case-study investigated, cables 5 and 7 (brown and cyan lines, respectively) possessed a very low tension while cables 1, 3,
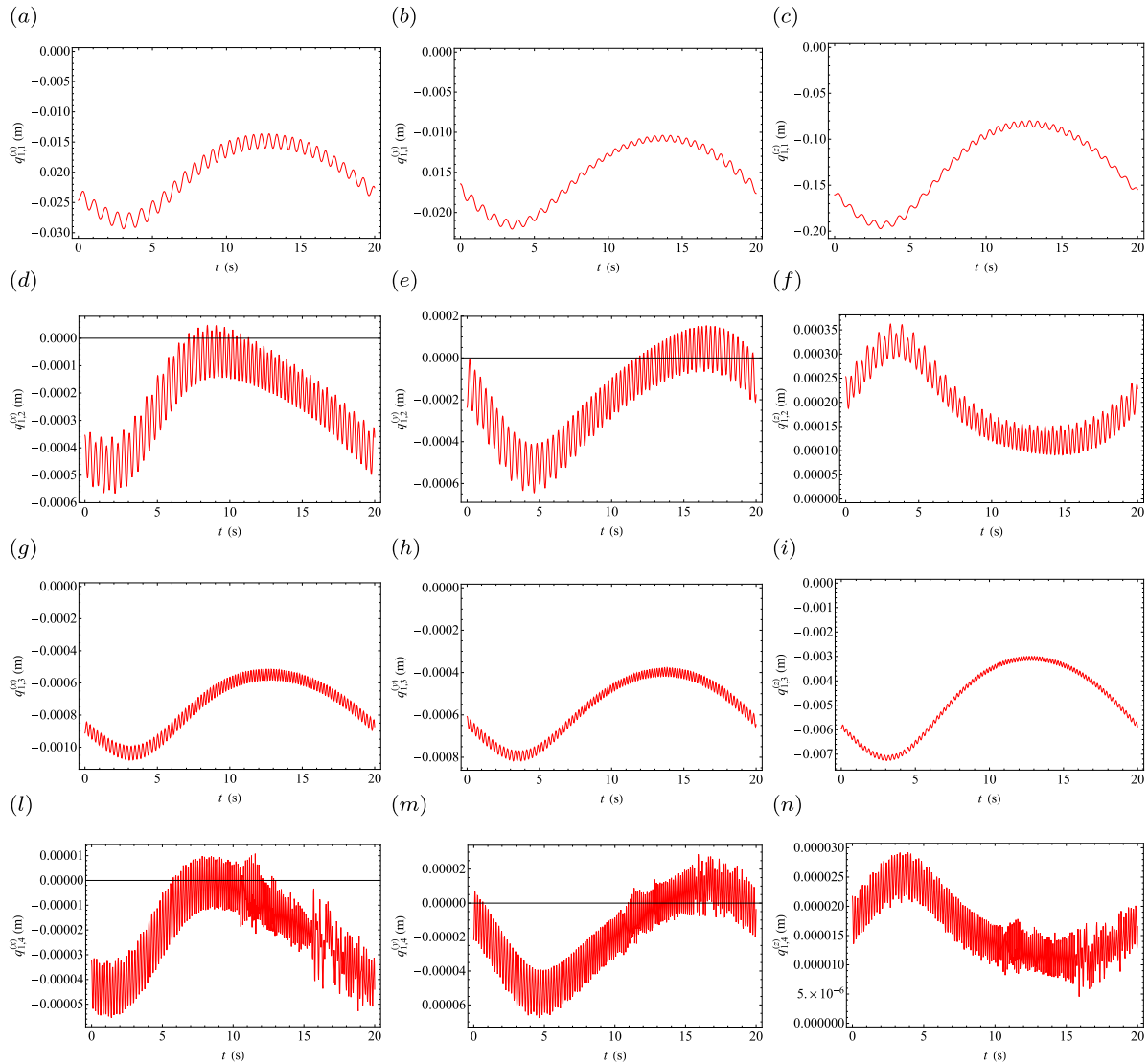
Fig. 17. Inverse approach, time history of the unknown generalized coordinates of cable 1: plots (*a*), (*d*), (*g*), and (*l*) show the components $q_{1,1}^{(x)}$, $q_{1,2}^{(x)}$, $q_{1,3}^{(x)}$, and $q_{1,4}^{(x)}$, respectively; plots (*b*), (*e*), (*h*), and (*m*) show the components $q_{1,1}^{(y)}$, $q_{1,2}^{(y)}$, $q_{1,3}^{(y)}$, and $q_{1,4}^{(y)}$, respectively; plots (*c*), (*f*), (*i*), and (*n*) show the components $q_{1,1}^{(z)}$, $q_{1,2}^{(z)}$, $q_{1,3}^{(z)}$, and $q_{1,4}^{(z)}$, respectively.

6, and 8, (red, green, yellow, and black lines, respectively) turned out to be the higher tensioned cables. This is due only to the choice of fixing in time the ratios $\Lambda_i(t)$ at the selected values approximately calculated as discussed in the previous sections. Finally, the configuration of the CDPM at selected time instants of the motion is shown in Fig. 20 together with close-up images of the end-effector configuration.

6. Conclusions

A parametric nonlinear dynamic model of CDPM undergoing three-dimensional motions was presented and discussed in this paper. Cables were modeled as elastic one-dimensional continua possessing distributed inertia and damping and characterized by time-varying length for the exact positioning (and orientation) in time of a three-dimensional end-effector mass. A solution strategy based on an *ad hoc* nondimensionalization of the system parameters and equations, and on the best choice of minimum admissible trial functions adopted to discretize the equations of motion of the cables, was proposed so as to overcome the analytical and numerical drawbacks related to the time-varying length of the cables. The particularization of the

mechanical problem to the case of point-mass end-effector and to the two-dimensional motion, respectively, was further provided. Finally, both the direct and the inverse dynamic problems were formulated and discussed in the case of minimally-actuated and over-actuated CDPM. Simulations were carried out on two case-studies to show the feasibility of the analytical model to investigate the dynamic response of an over-actuated CDPM via both, the direct, and the inverse approach. In particular, in the case of point-mass EE undergoing 3D circular uniform motion, the analyses carried out within the direct approach showed the importance of the discretization order of the solution of the equations of motion depending on the stress level possessed by the cables during the entire motion. Thus, it was highlighted that a small number of trial functions was sufficient also to describe the dynamics of moderately sagged cables (i.e., characterized by a moderately low pre-tension); therefore, it was shown that it is possible to appropriately describe the dynamics of CDPM by a low-order dynamical model which, thus, can be suitably adopted for designing optimal control strategies. On the other hand, the capability of the proposed model to study the 3D dynamics via an inverse approach, allowed to determine the effective motion of the EE and of the cables and, in particular, to claim that the
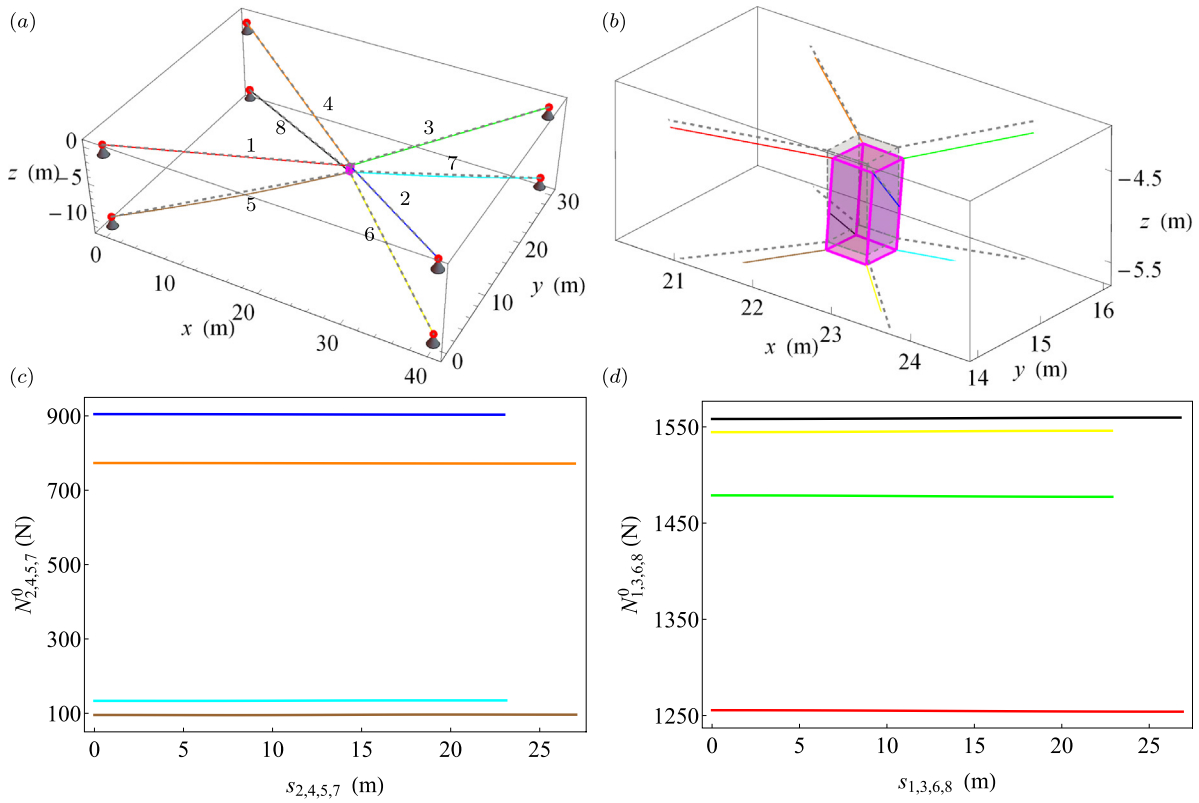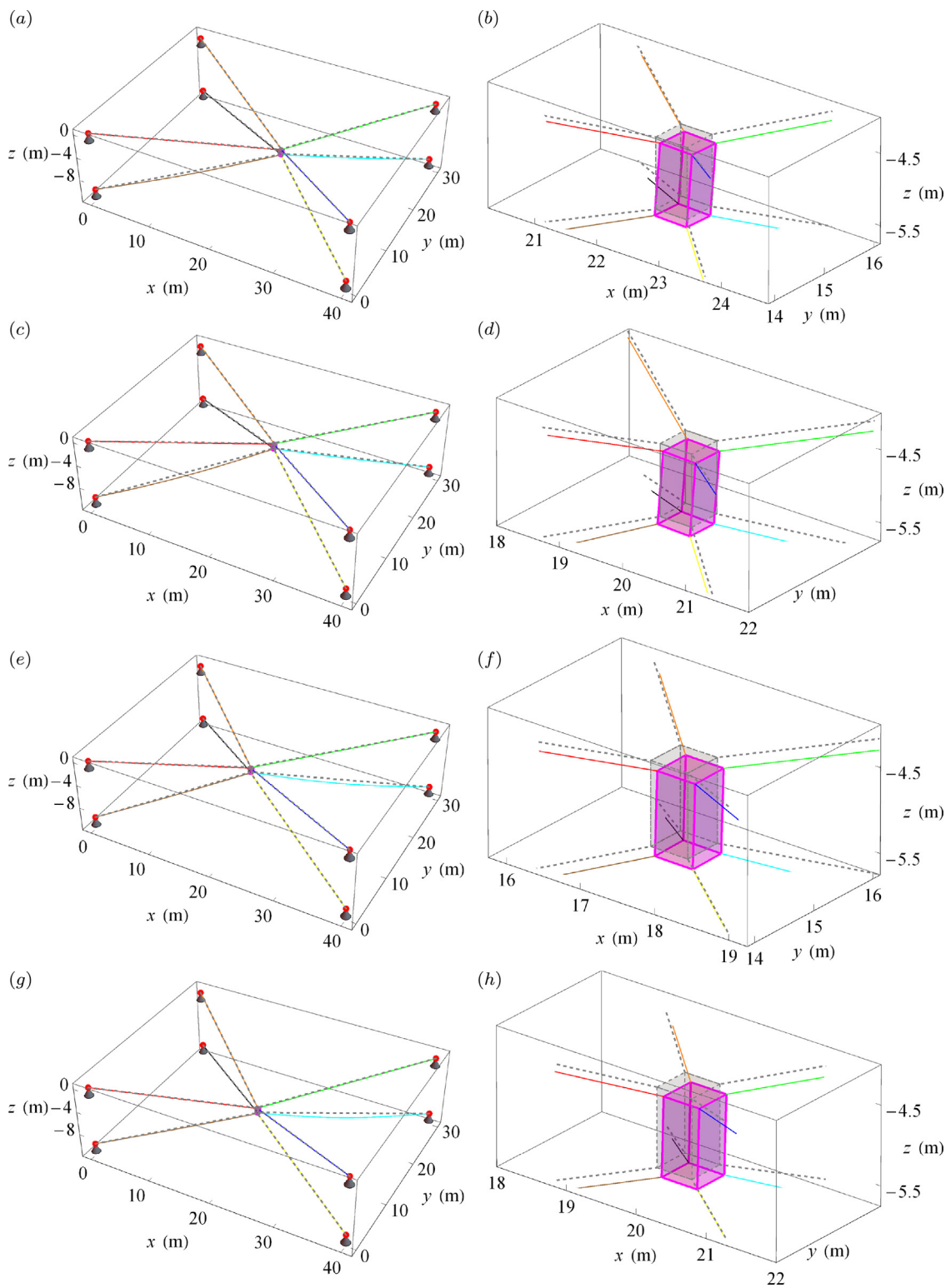
Fig. 18. Equilibrium configuration of the oriented mass EE along the selected trajectory at $t = 0$ (a), and close-up of the end-effector position and orientation (b). Axial forces in cables 2, 4, 5 and 7 (c) and in cables 1, 3, 6, and 8 (d) along the corresponding unstretched, dimensional, arclength s_i ($i = 1, \ldots, 8$). Red, blue, green, orange, brown, yellow, cyan, and black colors indicate cables 1, 2, 3, 4, 5, 6, 7 and 8, respectively. (For interpretation of the references to color in this figure legend, the reader is referred to the web version of this article.)
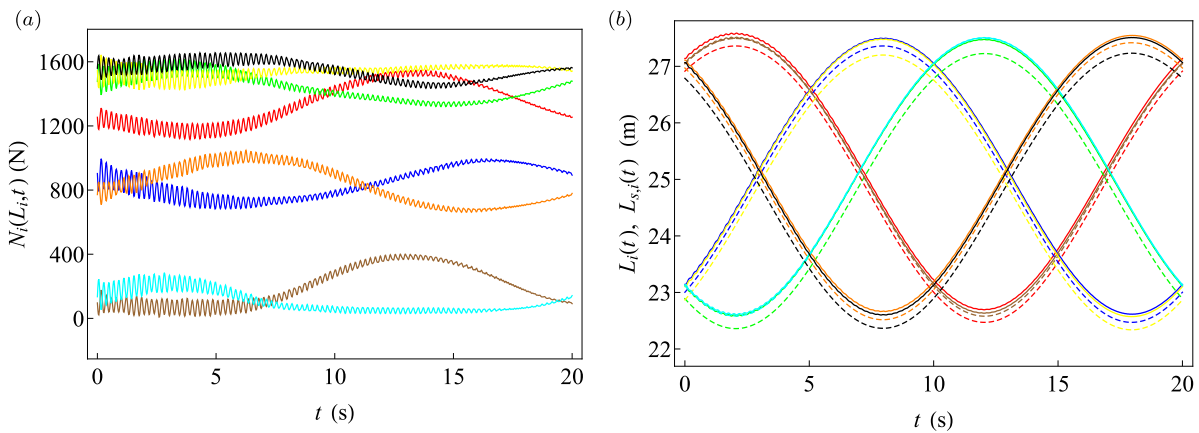
Fig. 19. Time variation of the cables' axial forces at $s_i = L_i(t)$ (a), and unstretched length $L_i(t)$ (solid lines) versus stretched length $L_{s,i}(t)$ (dashed lines) (b), for $i = 1, \ldots, 8$. Red, blue, green, orange, brown, yellow, cyan, and black colors indicate cables 1, 2, 3, 4, 5, 6, 7 and 8, respectively. (For interpretation of the references to color in this figure legend, the reader is referred to the web version of this article.)

dynamic configurations of all cables were characterized by two main frequencies: the first, corresponding to that of the assigned trajectory, and the second given by the lowest mode shape of each cable. This was due to the fact that, while in the direct approach the cables' aspect ratios are not effective values, since those are parameters assigned *a priori* and typically assumed constant in time, in the inverse dynamic problem those can be calculated as the solution of the equations of

motion and vary in time. Finally, a further case-study analysis was carried out to show the feasibility of the parametric model developed in this work to properly describe the 3D dynamics of a CDPM endowed with an oriented mass EE, both in terms of equilibrium and dynamic configurations, and in terms of the capability to recover the time histories of the axial forces along the cables' arclength and to monitor the change in time of the cables' length.

Fig. 20. Configurations of the oriented mass EE along the selected trajectory (*a*), (*c*), (*e*), (*g*), and close-up of the end-effector position and orientation (*b*), (*d*), (*f*), (*h*); each row corresponds to $t = 0, 5, 10, 15$ sec, respectively.

CRediT authorship contribution statement

Andrea Arena: Conceptualization, Methodology, Software, Validation, Formal analysis, Investigation, Resources, Data curation, Writing – original draft, Writing – review & editing, Visualization. **Erika Ottaviano:** Conceptualization, Methodology, Writing – review & editing, Visualization, Project administration, Funding acquisition. **Vincenzo Gattulli:** Conceptualization, Methodology, Writing – review & editing, Visualization, Project administration, Funding acquisition.

Declaration of competing interest

The authors declare that they have no known competing financial interests or personal relationships that could have appeared to influence the work reported in this paper.

Data availability

The data that has been used is confidential.

Acknowledgments

References

[1] J.-P. Merlet, Parallel Robots, vol. 128, Springer Science & Business Media, 2005.
[2] M. Gouttefarde, C.M. Gosselin, Analysis of the wrench-closure workspace of planar parallel cable-driven mechanisms, IEEE Trans. Robot. 22 (3) (2006) 434–445.
[3] M. Gouttefarde, D. Daney, J.-P. Merlet, Interval-analysis-based determination of the wrench-feasible workspace of parallel cable-driven robots, IEEE Trans. Robot. 27 (1) (2010) 1–13.
[4] S. Kawamura, W. Choe, S. Tanaka, H. Kino, Development of an ultrahigh speed robot FALCON using parallel wire drive systems, J. Robot. Soc. Jpn. 15 (1) (1997) 82–89.
[5] A. Gonzalez-Rodriguez, F. Castillo-Garcia, E. Ottaviano, P. Rea, A. Gonzalez-Rodriguez, On the effects of the design of cable-driven robots on kinematics and dynamics models accuracy, Mechatronics 43 (2017) 18–27.
[6] J. Albus, R. Bostelman, N. Dagalakis, The nist robocrane, J. Robot. Syst. 10 (5) (1993) 709–724.
[7] L.L. Cone, Skycam: An aerial robotic camera system, Byte 10 (10) (1985) 122–132.
[8] G. Castelli, E. Ottaviano, P. Rea, A Cartesian cable-suspended robot for improving end-users mobility in an urban environment, Robot. Comput.-Integr. Manuf. 30 (3) (2014) 335–343.
[9] J.-P. Merlet, Kinematics of the wire-driven parallel robot MARIONET using linear actuators, in: 2008 IEEE International Conference on Robotics and Automation, IEEE, 2008, pp. 3857–3862.
[10] B. Duan, Y. Qiu, F. Zhang, B. Zi, Analysis and experiment of the feed cable-suspended structure for super antenna, in: 2008 IEEE/ASME International Conference on Advanced Intelligent Mechatronics, IEEE, 2008, pp. 329–334.
[11] H.M. Irvine, Cable Structures, The MIT Press, 1981.
[12] N. Srinil, G. Rega, S. Chucheepsakul, Large amplitude three-dimensional free vibrations of inclined sagged elastic cables, Nonlinear Dynam. 33 (2) (2003) 129–154.
[13] M. Lepidi, V. Gattulli, F. Vestroni, Static and dynamic response of elastic suspended cables with damage, Int. J. Solids Struct. 44 (25–26) (2007) 8194–8212.
[14] A. Luongo, D. Zulli, Dynamic instability of inclined cables under combined wind flow and support motion, Nonlinear Dynam. 67 (1) (2012) 71–87.
[15] A. Arena, Free vibration of flexible cables, in: International Design Engineering Technical Conferences and Computers and Information in Engineering Conference, vol. 57181, American Society of Mechanical Engineers, 2015, V008T13A082.
[16] A. Arena, A. Pacitti, W. Lacarbonara, Nonlinear response of elastic cables with flexural–torsional stiffness, Int. J. Solids Struct. 87 (2016) 267–277.
[17] F. Foti, L. Martinelli, Mechanical modeling of metallic strands subjected to tension, torsion and bending, Int. J. Solids Struct. 91 (2016) 1–17.
[18] F. Foti, M. Geuzaine, V. Denoël, On the identification of the axial force and bending stiffness of stay cables anchored to flexible supports, Appl. Math. Model. 92 (2021) 798–828.
[19] M. Lepidi, V. Gattulli, Static and dynamic response of elastic suspended cables with thermal effects, Int. J. Solids Struct. 49 (9) (2012) 1103–1116.
[20] N. Riehl, M. Gouttefarde, S. Krut, C. Baradat, F. Pierrot, Effects of non-negligible cable mass on the static behavior of large workspace cable-driven parallel mechanisms, in: 2009 IEEE International Conference on Robotics and Automation, IEEE, 2009, pp. 2193–2198.
[21] J.-P. Merlet, The kinematics of cable-driven parallel robots with sagging cables: Preliminary results, in: 2015 IEEE International Conference on Robotics and Automation, ICRA, IEEE, 2015, pp. 1593–1598.
[22] K. Kozak, Q. Zhou, J. Wang, Static analysis of cable-driven manipulators with non-negligible cable mass, IEEE Trans. Robot. 22 (3).
[23] E. Ottaviano, A. Arena, V. Gattulli, F. Potenza, Slackening effects in 2D exact positioning in cable-driven parallel manipulators, in: A. Pott, T. Bruckmann (Eds.), Mechanisms and Machine Science, in: Cable-Driven Parallel Robots. CableCon 2019, vol. 74, Springer, Cham, 2019, pp. 319–330.
[24] E. Ottaviano, A. Arena, V. Gattulli, Geometrically exact three-dimensional modeling of cable-driven parallel manipulators for end-effector positioning, Mech. Mach. Theory 155 (104102) (2021) 1–20.
[25] S.-R. Oh, S.K. Agrawal, A reference governor-based controller for a cable robot under input constraints, IEEE Trans. Control Syst. Technol. 13 (4) (2005) 639–645.
[26] X. Diao, O. Ma, Vibration analysis of cable-driven parallel manipulators, Multibody Syst. Dyn. 21 (4) (2009) 347–360.
[27] S. Behzadipour, Stiffness of cable-based parallel manipulators with application to stability analysis, J. Mech. Des. 128 (1) (2006) 303–310.
[28] P. Tempel, P. Miermeister, A. Lechler, A. Pott, Modelling of kinematics and dynamics of the IPAnema 3 cable robot for simulative analysis, in: Applied Mechanics and Materials, vol. 794, Trans Tech Publ, 2015, pp. 419–426.
[29] H. Yuan, E. Courteille, D. Deblaise, Static and dynamic stiffness analyses of cable-driven parallel robots with non-negligible cable mass and elasticity, Mech. Mach. Theory 85 (2015) 64–81.
[30] Q. Wu, K. Takahashi, S. Nakamura, Formulae for frequencies and modes of in-plane vibrations of small-sag inclined cables, J. Sound Vib. 279 (2005) 1155–1169.
[31] X. Zhou, S. Yan, F. Chu, In-plane free vibrations of an inclined taut cable, J. Vib. Acoust. 133 (3).
[32] J. Du, C. Cui, H. Bao, Y. Qiu, Dynamic analysis of cable-driven parallel manipulators using a variable length finite element, J. Comput. Nonlinear Dyn. 10 (1).
[33] J. Du, S.K. Agrawal, Dynamic modeling of cable-driven parallel manipulators with distributed mass flexible cables, J. Vib. Acoust. 137 (2) (2015) 1–8.
[34] P. Tempel, D. Lee, F. Trautwein, A. Pott, Modeling of elastic-flexible cables with time-varying length for cable-driven parallel robots, in: A. Pott, T. Bruckmann (Eds.), Mechanisms and Machine Science, vol. 74, in: Cable-Driven Parallel Robots. CableCon 2019, Springer, Cham, 2019, pp. 295–306.
[35] M.R.J. Harandi, S.A. Khalilpour, H.D. Taghirad, J.G. Romero, Adaptive control of parallel robots with uncertain kinematics and dynamics, Mech. Syst. Signal Process. 157 (107693).
[36] W. Xu, P. Yan, F. Wang, H. Yuan, B. Liang, Vision-based simultaneous measurement of manipulator configuration and target pose for an intelligent cable-driven robot, Mech. Syst. Signal Process. 165 (108347).
[37] G. Meunier, B. Boulet, M. Nahon, Control of an overactuated cable-driven parallel mechanism for a radio telescope application, IEEE Trans. Control Syst. Technol. 17 (5) (2009) 1043–1054.
[38] Q. Duan, J. Du, B. Duan, T. Li, A. Tang, Modeling of variable length cable driven parallel robot, in: Proceedings of 2010 IEEE/ASME International Conference on Mechatronic and Embedded Systems and Applications, IEEE, 2010, pp. 545–548.
[39] M. Nahon, G. Gilardi, C. Lambert, Dynamics/control of a radio telescope receiver supported by a tethered aerostat, J. Guid. Control Dyn. 25 (6) (2002) 1107–1115.
[40] I. Adamiec-Wójcik, Ł. Drag, S. Wojciech, A new approach to the rigid finite element method in modeling spatial slender systems, Int. J. Struct. Stab. Dyn. 18 (02) (2018) 1850017.
[41] Z. Amare, B. Zi, S. Qian, J. Du, Q. Ge, Three-dimensional static and dynamic stiffness analyses of the cable driven parallel robot with non-negligible cable mass and elasticity, Mech. Based Des. Struct. Mach. 46 (4) (2018) 455–482.
[42] M. Michelin, C. Baradat, D.Q. Nguyen, M. Gouttefarde, Simulation and control with XDE and Matlab/Simulink of a cable-driven parallel robot (CoGiRo), in: Cable-Driven Parallel Robots, Springer, 2015, pp. 71–83.
[43] V. Ferravante, E. Riva, M. Taghavi, F. Braghin, T. Bock, Dynamic analysis of high precision construction cable-driven parallel robots, Mech. Mach. Theory 135 (2019) 54–64.
[44] H. Yuan, E. Courteille, M. Gouttefarde, P.-E. Hervé, Vibration analysis of cable-driven parallel robots based on the dynamic stiffness matrix method, J. Sound Vib. 394 (2017) 527–544.
[45] X. Zheng, T. Yang, Z. Chen, X. Wang, B. Liang, Q. Liao, ALE formulation for dynamic modeling and simulation of cable-driven mechanisms considering stick–slip frictions, Mech. Syst. Signal Process. 168 (108633).

[46] M. Koul, S.V. Shah, S. Saha, M. Manivannan, Reduced-order forward dynamics of multiclosed-loop systems, Multibody Syst. Dyn. 31 (4) (2014) 451–476.

[47] T.K. Mamidi, S. Bandyopadhyay, Forward dynamic analyses of cable-driven parallel robots with constant input with applications to their kinetostatic problems, Mech. Mach. Theory 163 (2021) 104381.

[48] S. Juárez-Pérez, A. Martí, A. Arena, E. Ottaviano, V. Gattulli, F.J. Castillo-Garcí, Dynamic control of a novel planar cable-driven parallel robot with a large wrench feasible workspace, Actuators 11 (367).

[49] Wolfram Research, Inc., Mathematica, Version 11, https://www.wolfram.com/mathematica, Champaign, IL, 2016.